nature immunology

ARTICLES

https://doi.org/10.1038/s41590-020-0596-6

Check for updates

Spatiotemporal regulation of type I interferon expression determines the antiviral polarization of CD4+ T cells

Marco De Giovanni[1,2], Valeria Cutillo[1,2], Amir Giladi[3], Eleonora Sala[1,2], Carmela G. Maganuco[1], Chiara Medaglia[3], Pietro Di Lucia[1], Elisa Bono[1], Claudia Cristofani[1], Eleonora Consolo[1,2], Leonardo Giustini[1], Alessandra Fiore[2], Sarah Eickhoff[4], Wolfgang Kastenmüller[4], Ido Amit[3], Mirela Kuka[1,2,6] ✉ and Matteo Iannacone[1,2,5,6] ✉

Differentiation of CD4+ T cells into either follicular helper T (T_{FH}) or type 1 helper T (T_H1) cells influences the balance between humoral and cellular adaptive immunity, but the mechanisms whereby pathogens elicit distinct effector cells are incompletely understood. Here we analyzed the spatiotemporal dynamics of CD4+ T cells during infection with recombinant vesicular stomatitis virus (VSV), which induces early, potent neutralizing antibodies, or recombinant lymphocytic choriomeningitis virus (LCMV), which induces a vigorous cellular response but inefficient neutralizing antibodies, expressing the same T cell epitope. Early exposure of dendritic cells to type I interferon (IFN), which occurred during infection with VSV, induced production of the cytokine IL-6 and drove T_{FH} cell polarization, whereas late exposure to type I IFN, which occurred during infection with LCMV, did not induce IL-6 and allowed differentiation into T_H1 cells. Thus, tight spatiotemporal regulation of type I IFN shapes antiviral CD4+ T cell differentiation and might instruct vaccine design strategies.

CD4+ T cells are key players in adaptive immune responses against pathogens. After priming in secondary lymphoid organs, antigen-specific CD4+ T cells undergo clonal expansion and differentiation into specialized effector T cell subsets. Viral infection may result in the generation of T_{FH} and T_H1 cells[1,2]. T_{FH} cells, which express the transcription factor Bcl-6, migrate into B cell follicles, where they promote the formation of high-affinity neutralizing antibodies[3,4]. T_H1 cells, which express the transcription factor T-bet[5], promote activation of macrophages and CD8+ T cell responses. As such, T_{FH} and T_H1 cell subsets contribute to adaptive immune responses by specifically supporting humoral and cellular immunity, respectively.

Although humoral and cellular immunity can be found in a state of 'competitive coexistence' (ref. [6]), one response usually emerges as dominant after viral infection and is responsible for most of the antiviral activity. Viruses that induce direct cell damage (cytopathic viruses), such as VSV, typically induce early, potent neutralizing antibody responses[7], whereas non-cytopathic viruses, such as LCMV, usually elicit robust cellular responses, but weak and inefficient neutralizing antibody responses[7]. The relative inefficiency of non-cytopathic viruses to induce neutralizing antibodies has been attributed, among other factors, to the properties of viral surface proteins, the frequency of germ line-encoded immunoglobulin variable regions, CD8+ T cell-induced immunopathological changes in secondary lymphoid organs and inflammatory monocyte-mediated suppression of B cells[7,8]. Here we investigated whether CD4+ T cell polarization had a role in the dichotomous responses to VSV and LCMV and characterized the spatiotemporal dynamics of the differentiation of antiviral CD4+ T cells. We found that CD4+ T cells differentiated mostly to T_{FH} cells upon infection with VSV and mostly to T_H1 cells upon infection with LCMV. Regardless of the differentiation outcome, priming of CD4+ T cells occurred in the outer paracortex and in the interfollicular areas of lymph nodes in both infections. The dichotomous T cell differentiation could not be explained by distinct cellular composition of the priming niches. Instead, spatiotemporal regulation of type I IFN expression determined whether dendritic cells (DCs) in the lymph node produced the cytokine IL-6 and, consequently, shaped antiviral CD4+ T cell polarization.

Results

VSV and LCMV induce distinct antiviral CD4+ T cell polarization. First, we compared CD4+ T cell polarization upon VSV or LCMV infection in C57BL/6 mice. We adoptively transferred naive VSV-specific (Tg7)[9] or LCMV-specific (SMARTA)[10] transgenic CD4+ T cells into C57BL/6 mice 24 h before subcutaneous intrafootpad infection with VSV Indiana (VSV Ind) or LCMV WE, respectively. CD4+ T cell polarization into Bcl-6+CXCR5+ T_{FH} cells and T-bet+CXCR5− T_H1 cells was analyzed at 3, 5, 7 and 14 d after infection in the footpad-draining popliteal lymph nodes (dLNs) (Extended Data Fig. 1a). On day 5 after VSV infection, >40% of Tg7 T cells had differentiated into T_{FH} cells, with little or no differentiation into T_H1 cells (Fig. 1a); at the same time point, >80% of SMARTA T cells were T_H1 cells and <15% had become T_{FH} cells (Fig. 1a). This pattern of CD4+ T cell polarization during VSV and LCMV infections was also observed when we analyzed

[1]Division of Immunology, Transplantation and Infectious Diseases, IRCCS San Raffaele Scientific Institute, Milan, Italy. [2]Vita-Salute San Raffaele University, Milan, Italy. [3]Department of Immunology, Weizmann Institute of Science, Rehovot, Israel. [4]Institute of Systems Immunology, Wurzburg, Germany. [5]Experimental Imaging Center, IRCCS San Raffaele Scientific Institute, Milan, Italy. [6]These authors contributed equally: Mirela Kuka, Matteo Iannacone. ✉e-mail: kuka.mirela@hsr.it; iannacone.matteo@hsr.it

the endogenous CD44^{hi}CD4$^+$ T cell response in the dLNs of mice subcutaneously infected with different viral strains (VSV Ind, VSV New Jersey, LCMV Armstrong, LCMV WE and LCMV clone 13) (Extended Data Fig. 1b,c) and occurred independently of the route of infection (intrafootpad or intravenous infection) (Extended Data Fig. 1d) and the size of the viral inoculum (10^2–10^7 plaque-forming units (p.f.u.) or focus-forming units (f.f.u.) per mouse) (Extended Data Fig. 1e).

T cell antigen receptor (TCR) signal strength influences CD4$^+$ T cell fate, with high-affinity antigen recognition associated with increased induction of T_{FH} cells[11]. To test whether the distinct CD4$^+$ T cell differentiation during VSV and LCMV infections was due solely to different TCR binding affinities, we infected C57BL/6 mice subcutaneously with recombinant VSV (rVSV) and LCMV (rLCMV) expressing glycoproteins containing the LCMV $gp_{61–80}$ epitope recognized by SMARTA CD4$^+$ T cells[12,13]. On day 5, >40% of SMARTA CD4$^+$ T cells had differentiated into T_{FH} cells during infection with rVSV, whereas >60% of these T cells became T_H1 cells upon infection with rLCMV (Fig. 1b,c and Extended Data Fig. 1f,g), indicating that features of the viral backbone dictated the cell fate of the CD4$^+$ T cells, independently of TCR affinity.

We next tested the localization and dynamic behavior of CD4$^+$ T cells in the LN by confocal immunofluorescence histology and intravital multiphoton microscopy (IVM). We imaged the dLNs of wild-type mice receiving CD4$^+$ T cells from Tg7 or SMARTA TCR-transgenic mice crossed with *Actb*-green fluorescent protein (GFP) mice on day 3 after infection with VSV Ind, rVSV or rLCMV. At this time point, we detected Tg7 and SMARTA T cells in the B cell follicles following infection with VSV Ind and rVSV, respectively (Fig. 1d,e); in contrast, SMARTA T cells in rLCMV-infected mice were confined outside the B cell follicles (Fig. 1d,e). The imaged Tg7 and SMARTA T cells had higher velocity and higher meandering index, an indicator of track straightness, in mice infected with VSV Ind and rVSV, respectively, than SMARTA T cells in mice infected with rLCMV (Fig. 1f,g, Extended Data Fig. 2a,b and Supplementary Video 1). These data indicate that VSV and LCMV induce distinct antiviral CD4$^+$ T cell polarization and in vivo dynamic behavior, independently of viral strain, viral dose, infection route and TCR signal strength.

Characterization of the antiviral CD4$^+$ T cell priming niche. Next, we characterized the precise location in the LN where priming and differentiation of antiviral CD4$^+$ T cells took place. CD4$^+$ T cell priming is thought to happen within the first 2 d following antigen administration in the outer paracortex and interfollicular areas of LNs[14–17]. In line with this, 48 h after infection with rVSV or rLCMV, SMARTA CD4$^+$ T cells had upregulated the activation markers CD69 and CD25 (Extended Data Fig. 2c,d) and migrated to the outer paracortex and interfollicular areas of infected LNs (Fig. 2a,b, Extended Data Fig. 2e and Supplementary Video 2), where they started to form clusters (Fig. 2a,c, Extended Data Fig. 2f and Supplementary Video 2). We refer to these areas as CD4$^+$ T cell 'priming niches' hereafter. To test whether the cellular and molecular composition of the niche supporting CD4$^+$ T cell priming differed between rVSV and rLCMV infections, we used NICHE-seq, which combines photoactivation and single-cell RNA sequencing (scRNA-seq) to spatially reconstruct immune niches[18]. We intravenously transferred CD4$^+$ T cells from SMARTA TCR-transgenic mice crossed with *Actb*-cyan fluorescent protein (CFP) mice into transgenic mice ubiquitously expressing photoactivatable GFP (PA-GFP)[19]; we then photoactivated areas in the dLNs containing SMARTA CD4$^+$ T cell clusters (that is, the outer paracortex and interfollicular areas) on day 2 after infection with rVSV or rLCMV and performed single-cell sorting to obtain 2,406 photoconverted total GFP$^+$ endogenous cells (Fig. 2d,e). scRNA-seq indicated that B cells and natural killer (NK) cells were over-represented in the samples from rVSV-infected mice, whereas CD8$^+$ T cells and CCR2$^+$ inflammatory monocytes were enriched in the samples from rLCMV-infected mice (Fig. 2e,f; cell subsets were identified on the basis of their gene expression signatures; Methods). Confocal microscopy indicated the presence of antigen-specific B cells, CX3CR1$^+$CCR2$^+$ cells, antigen-specific CD8$^+$ T cells and NKp46$^+$ cells in the CD4$^+$ T cell priming niche (Extended Data Fig. 3a–d).

B cells are required for the later stages of differentiation into T_{FH} cells[3]. To test whether a higher number of B cells in the CD4$^+$ T cell priming niche in VSV-infected mice drove differentiation into T_{FH} cells, we used VI10Yen mice, in which B cells express a transgenic B cell receptor (BCR) specific for an irrelevant antigen (VSV Ind glycoprotein)[20]. Adoptively transferred SMARTA CD4$^+$ T cells differentiated into T_{FH} cells and homed to B cell follicles similarly in

Fig. 1 | VSV and LCMV infections result in distinct antiviral CD4$^+$ T cell polarization and in vivo dynamics. a, Representative flow cytometry plots of transferred CD45.1$^+$ Tg7 CD4$^+$ T cells or CD45.1$^+$ SMARTA CD4$^+$ T cells (1×10^6 cells each) in the dLNs of CD45.2$^+$ wild-type recipient mice 5 d after intrafootpad infection with VSV Ind (left) or LCMV WE (right), respectively (see Extended Data Fig. 1a for a schematic of the experimental setup). Numbers indicate percentages within the indicated gates. Plots are representative of at least five independent experiments. **b**, Representative flow cytometry plots of transferred CD45.1$^+$ SMARTA CD4$^+$ T cells (1×10^6 cells) in the dLNs of CD45.2$^+$ wild-type recipient mice 5 d after intrafootpad infection with rVSV (left) or rLCMV (right). Numbers indicate percentages within the indicated gates. Plots are representative of at least five independent experiments. **c**, Quantification of T_{FH} cells (left) and T_H1 cells (right) as percentages of the transferred Tg7 (VSV Ind infection) or SMARTA (rVSV or rLCMV infection) CD45.1$^+$CD4$^+$ T cells in the dLNs of CD45.2$^+$ wild-type recipients at 0, 3, 5, 7 and 14 d after infection. The mean ± s.e.m. is shown. Day 0: $n=3$ (VSV) and 4 (rVSV and rLCMV); day 3: $n=5$ (VSV) and 7 (rVSV and rLCMV); day 5: $n=5$ (VSV), 9 (rVSV) and 10 (rLCMV); day 7: $n=3$ (all groups); day 14: $n=3$ (VSV and rVSV) and 6 (rLCMV). Black and blue stars indicate significance of VSV and rVSV samples, respectively, compared to rLCMV samples. Two-way ANOVA with least significant difference (LSD) post test was applied: $^*P<0.05$, $^{**}P<0.01$, $^{***}P<0.001$, $^{****}P<0.0001$. **d**, Confocal micrographs of dLNs in wild-type mice injected with 1×10^6 purified GFP$^+$ Tg7 (VSV Ind) or SMARTA (all other groups) CD4$^+$ T cells (green) and 3×10^7 purified Deep Red-labeled polyclonal B cells (gray) 1 d before injection with PBS, VSV Ind, rVSV or rLCMV. The images on the bottom are the same as the images on the top except that the channel pertaining to polyclonal B cells was removed to improve clarity. Images were collected 3 d after infection and are representative of at least three independent experiments. Scale bars, 200 µm. **e**, Quantification of follicular antigen-specific CD4$^+$ T cells in the dLNs of mice shown in **d**. The mean ± s.e.m. is shown. $n=2$ (PBS) and 4 (VSV Ind, rVSV and rLCMV). One-way ANOVA with Bonferroni's post test was applied: $^{***}P<0.001$. **f**, Snapshots from multiphoton intravital imaging of dLNs in wild-type mice injected with 1×10^6 purified GFP$^+$ Tg7 (VSV Ind) or SMARTA (all other groups) CD4$^+$ T cells (green) and 3×10^7 purified Deep Red-labeled polyclonal B cells (gray), injected 1 d before injection with PBS, VSV Ind, rVSV or rLCMV (Supplementary Video 1). Cell tracks are colored according to mean values for track speed (blue, 0 µm s^{-1}; red, 1 µm s^{-1}; Supplementary Video 1). Dashed lines define B cell follicles and are depicted on the basis of polyclonal B cell positioning. Scale bars, 50 µm. Data are representative of at least two independent experiments. **g**, Intravital cytometry plots of the videos in **f** showing Tg7 (VSV Ind) or SMARTA (all other groups) CD4$^+$ T cell *xy* cell positions over time (top) and meandering index versus mean track speed (bottom; Supplementary Video 1). Gates represent percentages of follicular CD4$^+$ T cell tracks (top) and CD4$^+$ T cell tracks with a high meandering index and high mean track speed (bottom). Numbers indicate the percentage of tracks within the indicated gates. Data are representative of at least two independent experiments.

wild-type and VI10Yen mice after infection with rVSV (Fig. 2g and Extended Data Fig. 4a), indicating that antigen-specific B cells were not needed for the initial differentiation of CD4+ T cells. NK cells have been reported to curtail virus-specific CD4+ T cell responses, including T_{FH} cell responses, during chronic viral infection[21]. However, depletion of NKp46+ cells, including NK cells, in *Ncr1*-Cre;

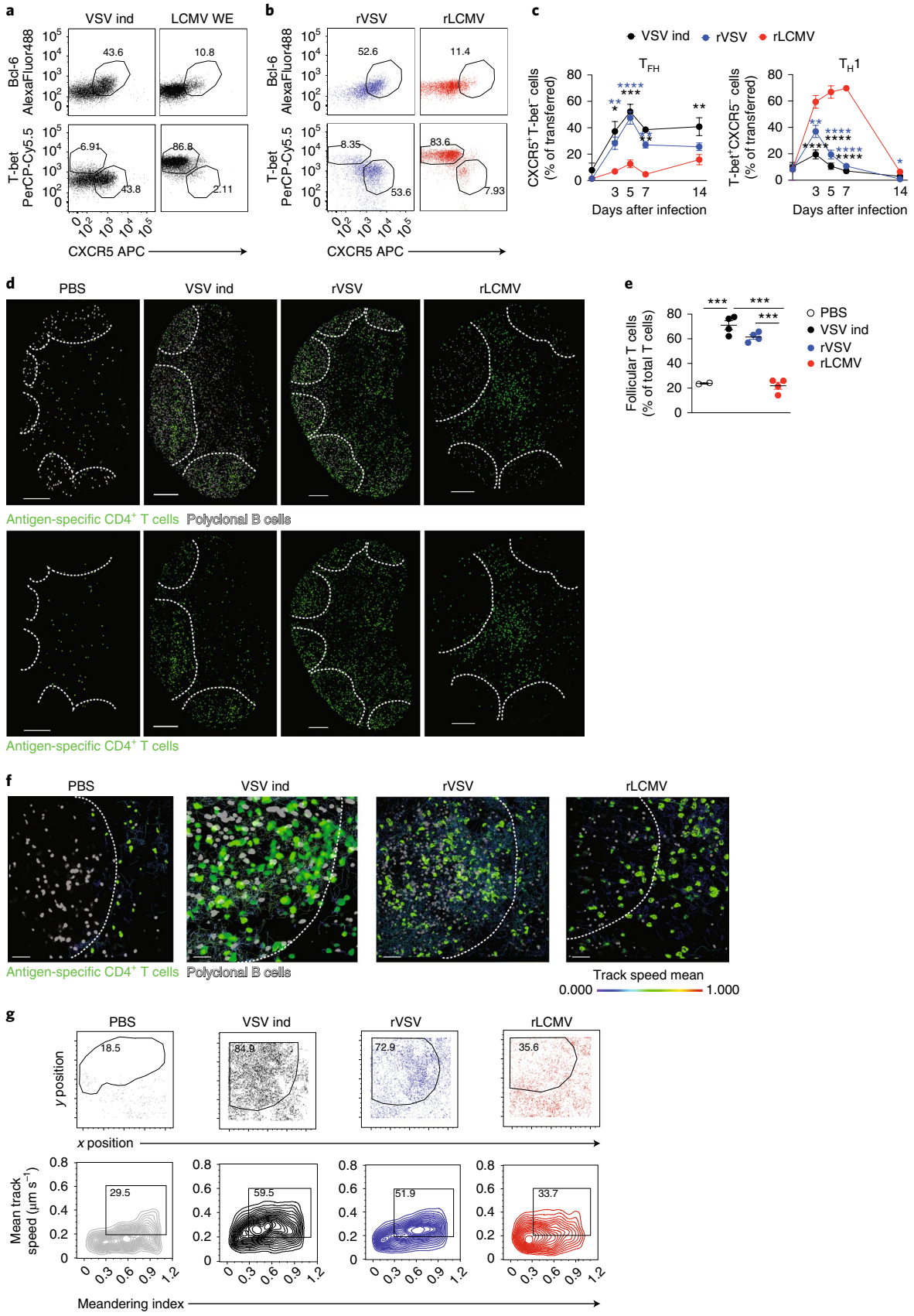

Rosa26-iDTR mice (where *Ncr1* corresponds to the promoter for the gene encoding NKp46)[22,23] injected with diphtheria toxin indicated that NK cells were dispensable for early SMARTA CD4$^+$ T cell differentiation upon rVSV or rLCMV infection (Extended Data Fig. 5a–c). Immunopathological changes in secondary lymphoid organs or direct killing of B cells by CD8$^+$ T cells can subvert B cell responses[8,24–26]. Use of Cor93 transgenic recipient mice, in which T cells bear a TCR specific for an irrelevant antigen (the hepatitis B virus core protein)[27], indicated that antigen-specific CD8$^+$ T cells were not required for the early polarization of SMARTA CD4$^+$ T cells upon rVSV or rLCMV infection (Fig. 2h and Extended Data Fig. 4b). Recruitment of CCR2$^+$ inflammatory monocytes to LCMV-infected LNs was shown to hinder LCMV-specific B cell responses[8,28]. However, *Ccr2*$^{-/-}$ recipient mice, in which monocytes cannot migrate to infected LNs[28,29], were indistinguishable from wild-type mice in their ability to support early SMARTA CD4$^+$ T cell differentiation upon rVSV or rLCMV infection (Fig. 2i and Extended Data Fig. 4c).

Priming of naive CD4$^+$ T cells within LNs is mediated by mature conventional dendritic cells (cDCs), which present antigen and deliver co-stimulatory stimuli and cytokines[14,15,17,30]. cDCs were detected in the T_{FH} cell and T_H1 cell priming niches by NICHE-seq (Fig. 2e,f), but the relative paucity of these cells among the photoactivated cells prevented their detailed phenotypic characterization. The membrane receptor ICOSL is sensitive to ICOS-induced shedding during interactions with activated ICOS^{hi} T cells[31]. To determine the DC subsets that interacted with CD4$^+$ T cells upon VSV or LCMV infection, we measured the expression of ICOSL on CD11c$^+$ major histocompatibility complex class II (MHC-II)^{hi} DCs in rVSV- and rLCMV-infected mice treated with a blocking antibody against ICOS, as an indirect indicator of the interaction between LN DCs and cognate T cells. In both rVSV- and rLCMV-infected mice, CD11c$^+$MHC-II^{hi}CD11b$^+$ cDC2s, but not CD11c$^+$MHC-II^{hi}CD8$^+$ cDC1s, had increased expression of ICOSL (Extended Data Fig. 5d,e), suggesting that interactions between cDC2s and cognate CD4$^+$ T cells drive the differentiation of both T_{FH} and T_H1 cells. In addition, SMARTA CD4$^+$ T cells transferred into *Xcr1*-DTR mice, in which cDC1s were depleted by diphtheria toxin injection starting 2 d before infection, differentiated normally into T_{FH} or T_H1 cells upon rVSV and rLCMV infection, respectively (Extended Data Fig. 5f). Thus, the differences in helper T cell polarization observed during infection with VSV and LCMV were due to priming by DC subsets other than cDC1s, possibly exposed to a different local cytokine milieu.

Spatiotemporal regulation of type I IFN expression determines CD4$^+$ T cell polarization. Next, we analyzed the transcriptome of cells in the photoactivated CD4$^+$ T cell priming niche of rVSV- and rLCMV-infected mice. NICHE-seq analysis indicated an increased type I IFN signature in cells isolated from the CD4$^+$ T cell priming niche of rLCMV-infected mice as compared to cells from the CD4$^+$ T cell priming niche of rVSV-infected mice on day 2 after infection (Fig. 3a). Although sensing of type I IFN is known to influence CD4$^+$ T cell polarization, the effect of type I IFN on the activation and differentiation of antiviral CD4$^+$ T cells remains poorly defined, with conflicting reports, possibly depending on the context of infection. Kinetic analysis of *Ifna2*, *Ifna5*, *Ifna6*, *Ifna7*, *Ifna9*, *Ifna12*, *Ifna13*, *Ifna14*, *Ifnb* and two representative IFN-stimulated genes (ISGs), *Isg15* and *Oas2*, in total RNA isolated from LNs at 4, 8, 16, 24 and 48 h after infection with rVSV or rLCMV indicated that, although the magnitude of type I IFN induction did not significantly differ between rVSV and rLCMV infection, rVSV induced an earlier wave of type I IFN, which peaked at 8 h after infection, whereas rLCMV induced a delayed (24 h) and prolonged peak (Fig. 3b and Extended Data Fig. 6), possibly reflecting the different kinetics of viral replication in vivo[28]. REX3 reporter mice express red fluorescent protein (RFP) and blue fluorescent protein (BFP) under the control of the promoters of the ISGs *Cxcl9* and *Cxcl10*, respectively[17]. We detected stronger expression of *Cxcl9*-RFP and *Cxcl10*-BFP in the outer paracortex, cortical ridge and interfollicular areas in the LNs of rVSV-infected REX3 mice as compared to rLCMV-infected mice 12 h after infection, corresponding to areas where SMARTA CD4$^+$ T cells accumulated (Fig. 3c).

To test the effect of the two profiles of type I IFN induction on the differentiation of CD4$^+$ T cells, we transferred SMARTA CD4$^+$ T cells into wild-type mice and treated them with an antibody that blocks signaling through the type I IFN receptor (IFNAR1) 1 d before infection with rVSV or rLCMV. Whereas CD4$^+$ T cells transferred in IFNAR1-blocked rLCMV-infected mice differentiated into T_H1 cells, induction of T_{FH} cells in rVSV-infected mice was severely compromised, with transferred CD4$^+$ T cells differentiating into T-bet$^+$CXCR5$^-$ T_H1 cells, which were excluded from B cell follicles and induced fewer germinal center B cells and GP-specific IgG1 antibodies (Fig. 3d,e, Extended Data Fig. 7a,b and Supplementary Video 3), suggesting that type I IFN affected CD4$^+$ T cell polarization at early time points after infection. Administration of the blocking antibodies against IFNAR1 on day 1 after rVSV infection did not affect the differentiation of SMARTA cells into T_{FH} cells in comparison to untreated controls (Fig. 3f and Extended Data Fig. 7c), indicating that type I IFN sensing within the first 24 h after infection was essential for the induction of T_{FH} cells. To assess whether an early wave of type I IFN increased the differentiation of

Fig. 2 | Characterization of the antiviral CD4$^+$ T cell priming niche. a, Confocal micrographs of dLNs in mice injected with 5×10^6 purified GFP$^+$ antigen-specific (SMARTA) CD4$^+$ T cells (green) and 3×10^7 purified Deep Red-labeled polyclonal B cells (gray) 1 d before injection with PBS, rVSV or rLCMV. Images were acquired 2 d after infection and are representative of at least two independent experiments. The top panels depict the positioning of GFP$^+$ antigen-specific (SMARTA) T cells, while the bottom panels indicate the clustered antigen-specific (SMARTA) T cells (purple). A T cell cluster was defined as a minimum of three T cells within a distance of 15 µm measured from the centroid of each cell (Methods). Scale bars, 200 µm. See also Supplementary Video 2. **b**,**c**, Quantification of the normalized distance of antigen-specific (SMARTA) T cells from the T cell area center (**b**) and percentage of clustered T cells per section (**c**) in the mice described in **a**. The mean ± s.e.m. is shown. In **b**, $n=772$ (PBS), 1,025 (rVSV) and 1,127 (rLCMV) cells; in **c**, $n=3$ (PBS), 5 (rVSV) and 4 (rLCMV) sections. Results were pooled from two independent experiments. One-way ANOVA with Bonferroni's post test was applied: $^*P<0.05$, $^{****}P<0.0001$. **d**, Multiphoton intravital micrographs depicting photoactivation of the CD4$^+$ T cell priming niche upon rVSV or rLCMV infection. Images were acquired 2 d after infection. Antigen-specific (SMARTA) CFP$^+$CD4$^+$ T cells are depicted in green, and PA-GFP$^+$ cells are depicted in blue. Top, before photoactivation; bottom, after photoactivation. Scale bars, 50 µm. Images are representative of at least two independent experiments. **e**, Gene expression profiles of 2,406 single cells from photoactivated priming niches, grouped in seven clusters. The color bar indicates each cell's origin (blue, photoactivated cells from rVSV-infected mice; red, photoactivated cells from rLCMV-infected mice). UMI, unique molecular identifier. **f**, Relative abundance of different cell clusters within CD4$^+$ T cell priming niches. Data represent cell counts from two biological replicates. Two-sided false discovery rate (FDR)-adjusted Fisher's exact test: $^*P<0.05$, $^{***}P<0.001$, $^{****}P<0.0001$. **g–i**, 1×10^6 purified CD45.1$^+$ antigen-specific (SMARTA) CD4$^+$ T cells were injected into CD45.2$^+$ wild-type (WT) recipients and into VI10YEN (**g**; $n=6$), Cor93 TCR-transgenic (Tg) (**h**; $n=4$ or 6) and *Ccr2*$^{-/-}$ (**i**; $n=4$ or 6) mice. dLNs were collected 3 d (**g**) or 5 d (**h**,**i**) after rVSV (blue) or rLCMV (red) infection. Percentages of T_{FH} (**g–i**, left) and T_H1 (**h**,**i**, right) antigen-specific CD4$^+$ T cells out of total transferred cells in dLNs were quantified by flow cytometry. Data are representative of at least two independent experiments. The mean ± s.e.m. is shown. One-way ANOVA with Bonferroni's post test was applied: $^{**}P<0.01$, $^{***}P<0.001$.

T_{FH} cells in LCMV-infected mice, we injected poly(I:C), which binds TLR3 to induce type I IFN, simultaneously with rLCMV. On day 5 after infection, we observed a significant increase in T_{FH} cell differentiation and a reduction in T_H1 cells in the LNs of poly(I:C)-treated mice as compared to untreated mice (Fig. 3g). Together, these results indicate that early (<24 h) type I IFN sensing drives T_{FH} cell differentiation.

Early type I IFN sensing by DCs and IL-6 are essential for T_{FH} cell differentiation. Type I IFN sensing by different cell types has been reported to influence CD4$^+$ T cell differentiation in a variety of experimental settings, with data pointing to a stimulatory or inhibitory role in the polarization toward T_{FH} and/or T_H1 cells[32]. To investigate the role of type I IFN receptor signaling in CD4$^+$ T cells, we adoptively transferred wild-type or *Ifnar1*$^{-/-}$ SMARTA CD4$^+$

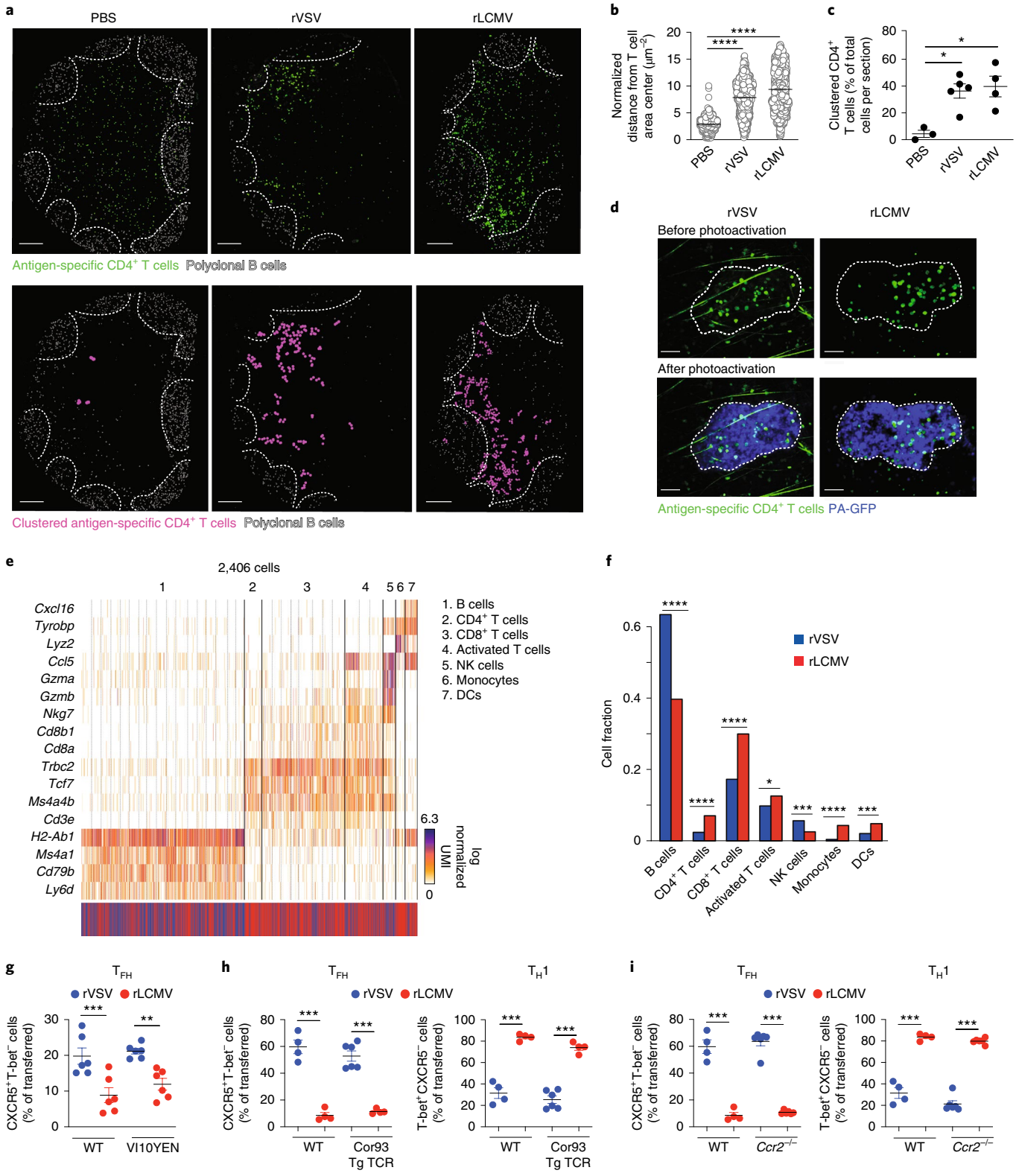

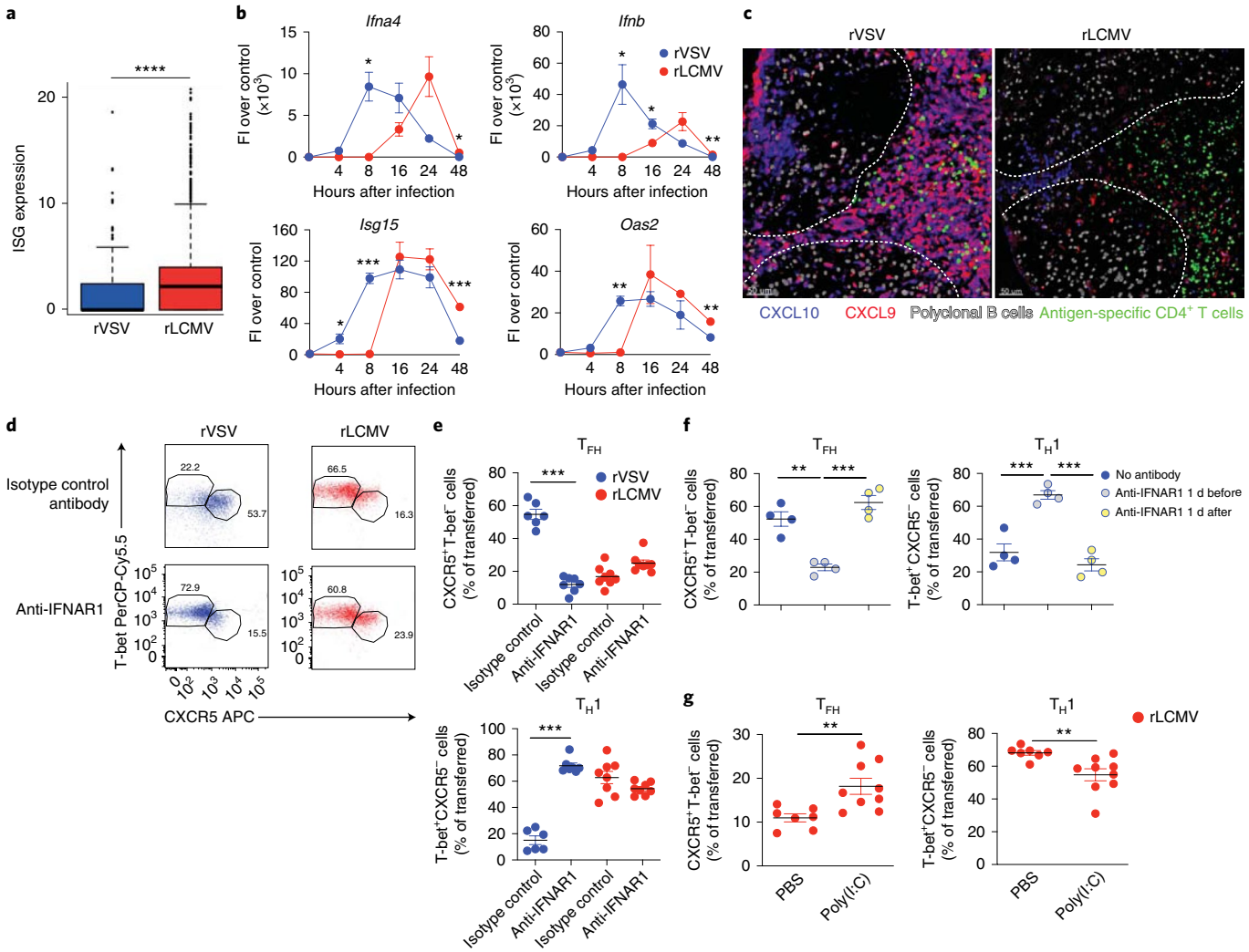

Fig. 3 | Spatiotemporal regulation of type I IFN expression determines antiviral CD4⁺ T cell polarization. a, Expression profile of selected ISGs (*Irf7*, *Cxcl9*, *Cxcl10*, *Oasl1*, *Ifitm3*, *Oas2* and *Isg15*) in 2,406 single cells from the photoactivated CD4⁺ T cell priming niches described in Fig. 2d–f. Data were pooled from two independent experiments. Kolmogorov–Smirnov test was applied: $^{****}P < 0.0001$. **b**, Analysis of *Ifna4*, *Ifnb*, *Isg15* and *Oas2* gene expression in dLN at 0, 4, 8, 16, 24 and 48 h after rVSV (blue) or rLCMV (red) infection by qPCR. $n = 3$ (0 h), 4 (4 h), 4 (8 h), 4 (16 h), 3 (24 h, rLCMV), 4 (24 h, rVSV) and 4 (48 h). Data were pooled from two independent experiments. The mean ± s.e.m. is shown. Two-way ANOVA with LSD post test was applied: $^{*}P < 0.05$, $^{**}P < 0.01$, $^{***}P < 0.001$. The same sample was measured repeatedly for the four genes. FI, fold increase. **c**, Confocal micrographs of dLNs in REX3 reporter mice injected with 1×10^7 purified GFP⁺ antigen-specific (SMARTA) CD4⁺ T cells (green) and 3×10^7 purified Deep Red-labeled polyclonal B cells (gray), 12 h after rVSV or rLCMV infection. CXCL10⁺ (blue) and CXCL9⁺ (red) cells are depicted. Data are representative of at least two independent experiments. **d**, Representative flow cytometry plots showing T_{FH} and T_H1 cells among antigen-specific CD4⁺ T cells, 5 d after infection of CD45.2⁺ wild-type recipients injected with 1×10^6 purified CD45.1⁺ SMARTA CD4⁺ T cells and treated with anti-IFNAR1 blocking antibody (or isotype control) 1 d before rVSV (blue, left) or rLCMV (red, right) infection. Numbers represent the percentage of cells within the indicated gate. **e**, Quantification of T_{FH} (top) and T_H1 (bottom) cells, expressed as percentages of antigen-specific CD4⁺ T cells out of total transferred cells, in dLNs of the mice described in **d**. The mean ± s.e.m. is shown. $n = 6$ (rVSV) and 8 (rLCMV). Data are representative of at least two independent experiments. One-way ANOVA with Bonferroni's post test was applied: $^{***}P < 0.001$. **f**, Quantification of the percentages of T_{FH} (left) and T_H1 (right) antigen-specific CD4⁺ T cells (out of total transferred cells) in dLNs 5 d after infection of CD45.2⁺ wild-type recipients injected with 1×10^6 purified CD45.1⁺ antigen-specific (SMARTA) CD4⁺ T cells and treated with anti-IFNAR1 blocking antibody either 1 d before (light blue) or 1 d after (yellow) rVSV infection. Data are representative of at least two independent experiments. The mean ± s.e.m. is shown; $n = 4$. One-way ANOVA with Bonferroni's post test was applied: $^{**}P < 0.01$, $^{***}P < 0.001$. **g**, Quantification of the percentages of T_{FH} (left) and T_H1 (right) antigen-specific CD4⁺ T cells (out of total transferred cells) in dLNs 5 d after infection of CD45.2⁺ wild-type recipients injected with 1×10^6 purified CD45.1⁺ antigen-specific (SMARTA) CD4⁺ T cells, infected with rLCMV and treated or not with poly(I:C). Data are representative of at least two independent experiments; $n = 7$ (PBS) and 9 (poly(I:C)). An unpaired two-tailed *t* test was applied: $^{**}P < 0.01$.

T cells into wild-type recipients 1 d before rVSV infection. On day 5 after infection, we observed no differences between wild-type and *Ifnar1*$^{-/-}$ SMARTA T cell differentiation into T_{FH} or T_H1 cells (Fig. 4a), indicating that intrinsic type I IFN sensing by CD4⁺ T cells is dispensable for CD4⁺ T cell differentiation. We next investigated the role of type I IFN sensing in DCs, which had the most upregulated expression of ISGs in the CD4⁺ T cell priming niche (Extended Data Fig. 8). Wild-type SMARTA CD4⁺ T cells adoptively transferred into irradiated wild-type mice reconstituted with bone marrow from *Cd11c*-Cre; *Ifnar1*$^{fl/fl}$ mice 8 weeks before CD4⁺ T cell

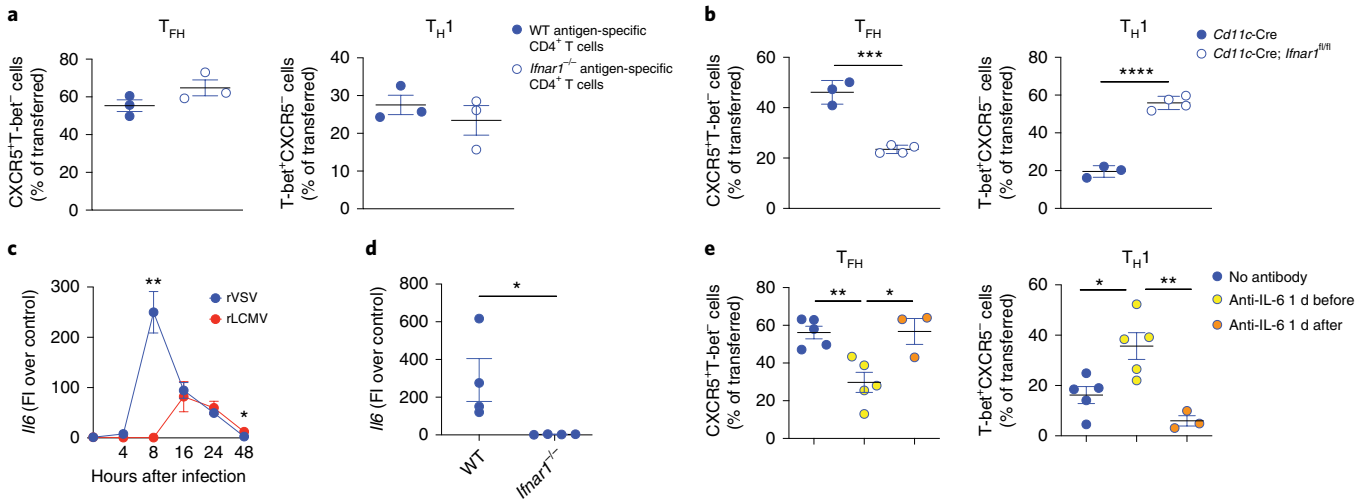

Fig. 4 | Early type I IFN sensing by DCs and IL-6 are essential for antiviral T_{FH} differentiation. a, Quantification of the percentages of T_{FH} and T_H1 antigen-specific CD4+ T cells (out of total transferred cells) in dLNs 5 d after rVSV infection of CD45.2+ wild-type mice injected with 1×10^6 purified CD45.1+ wild-type or *Ifnar1*$^{-/-}$ antigen-specific (SMARTA) CD4+ T cells. The mean ± s.e.m. is shown. $n=3$. **b**, Quantification of the percentages of T_{FH} and T_H1 antigen-specific (SMARTA) CD4+ T cells (out of total transferred cells) in dLNs 5 d after rVSV infection of either CD45.2+ *Cd11c*-Cre or CD45.2+ *Cd11c*-Cre; *Ifnar1*$^{fl/fl}$ recipients injected with 1×10^6 purified CD45.1+ antigen-specific (SMARTA) CD4+ T cells. dLNs were collected 5 d after rVSV infection. Data are representative of three independent experiments. The mean ± s.e.m. is shown. *Cd11c*-Cre, $n=3$; *Cd11c*-Cre; *Ifnar1*$^{fl/fl}$, $n=4$. An unpaired two-tailed *t* test was applied: ***$P<0.001$, ****$P<0.0001$. **c**, qPCR analysis of the *Il6* gene expression profile at 0, 4, 8, 16, 24 and 48 h in dLNs of mice infected with rVSV (blue) or rLCMV (red). The mean ± s.e.m. is shown. $n=4$ (0 h), 4 (4 h), 4 (8 h), 4 (16 h), 3 (24 h, rLCMV), 4 (24 h, rVSV) and 4 (48 h). Data were pooled from two independent experiments. Two-way ANOVA with LSD post test was applied: *$P<0.05$, **$P<0.01$. **d**, qPCR analysis of *Il6* gene expression in wild-type and *Ifnar1*$^{-/-}$ mice in dLNs 8 h after rVSV infection. Data were pooled from two independent experiments. The mean ± s.e.m. is shown. An unpaired two-tailed *t* test was applied: *$P<0.05$. **e**, Quantification of the percentages of T_{FH} (left) and T_H1 (right) antigen-specific CD4+ T cells (out of total transferred cells) in CD45.2+ wild-type recipients injected with 1×10^6 purified CD45.1+ antigen-specific (SMARTA) CD4+ T cells and treated with anti-IL-6 blocking antibody starting either 1 d before (yellow) or 1 d after (orange) rVSV infection. Data are representative of at least two independent experiments. The mean ± s.e.m. is shown. No antibody, $n=5$; anti-IL-6 1 d before, $n=5$; anti-IL-6 1 d after, $n=3$. One-way ANOVA with Bonferroni's post test was applied: *$P<0.05$, **$P<0.01$.

transfer showed significantly impaired differentiation into T_{FH} cells on day 5 after rVSV infection (Fig. 4b), indicating that type I IFN sensing by DCs is essential for antiviral T_{FH} induction.

IL-6 is known to promote early T_{FH} differentiation[33,34], and its induction is known to be dependent on type I IFN[35]. Kinetic analysis of *Il6* expression in LNs from wild-type mice infected with rVSV or rLCMV indicated that induction of *Il6* mRNA had an early peak (8 h after infection) during VSV infection and a delayed (>16 h) and lower peak during LCMV infection (Fig. 4c), mirroring the type I IFN signature. *Ifnar1*$^{-/-}$ mice had no upregulation of *Il6* mRNA 8 h after rVSV infection (Fig. 4d), indicating that the VSV-induced early expression of *Il6* requires type I IFN sensing. Blocking IL-6 before, but not 24 h after, rVSV infection significantly impaired induction of T_{FH} cells and virus-specific antibody titers and increased induction of T_H1 cells (Fig. 4e and Extended Data Fig. 9a,b), whereas it did not affect T helper cell polarization upon rLCMV infection (data not shown). These observations identify IL-6 as a critical early determinant of the differentiation of antiviral T_{FH} cells.

To determine whether type I IFN induced expression of IL-6 in DCs, we assessed the composition and transcriptional state of DC subsets after early and late type I IFN sensing. scRNA-seq on 2,179 CD11c+MHC-II^{hi} DCs passing quality control sorted from the LNs of wild-type or *Ifnar1*$^{-/-}$ mice at 8 or 48 h after infection with rVSV or rLCMV and unbiased analysis using the MetaCell package[36] indicated that CD11c+MHC-II^{hi} DCs could be subsetted into migratory cDC2s, cDC1s, cDC2s, monocyte-derived DCs (moDCs) and a small subset of contaminant macrophages (Fig. 5a). Experimental conditions where type I IFN signaling was maximal (that is, 8 h after rVSV infection and 48 h after rLCMV infection of wild-type mice as compared to the same time points in *Ifnar1*$^{-/-}$ mice or 8 h after rLCMV infection) showed an enrichment of DC subsets (migratory cDC2s and moDCs) that can support T_{FH} cell differentiation (Fig. 5b)[37]. Furthermore, ISGs induced by type I IFN were upregulated in DCs from wild-type, but not *Ifnar1*$^{-/-}$, mice, particularly in experimental conditions (8 h after rVSV and 48 h after rLCMV infection) where type I IFN signaling was maximal (Fig. 5c,d and Extended Data Fig. 10), indicating that DCs responded to type I IFN. Notably, migratory cDC2s and moDCs produced *Il6* at 8 h after rVSV infection of wild-type but not *Ifnar1*$^{-/-}$ mice (Fig. 5e); by contrast, after rLCMV infection, *Il6* mRNA had very low expression in migratory cDC2s and moDCs from wild-type and *Ifnar1*$^{-/-}$ mice, even at 48 h after infection when other ISGs were maximally induced (Fig. 5e). Thus, DCs produce *Il6* and drive T_{FH} cell polarization in response to early (rVSV) but not late (rLCMV) type I IFN signaling.

Discussion

Here we identified tight spatiotemporal regulation of the expression of type I IFN as a critical determinant of CD4+ T cell fate upon viral infection. When DCs were exposed to an early (<24 h) wave of type I IFN, they made IL-6, thus promoting the differentiation of T_{FH} cells and, consequently, enhancing humoral immunity; in contrast, when DCs were exposed to late type I interferon (>24 h), they no longer produced IL-6 and CD4+ T cells differentiated into a non-T_{FH} cell fate. These results might explain why many non-cytopathic, slow-replicating viruses fail to induce or interfere with the generation of neutralizing antibodies[7,8].

The notion that type I IFN influences the differentiation of CD4+ T cells is not without precedent[32]. However, the role of type I IFN in CD4+ T cell polarization has remained controversial. While some

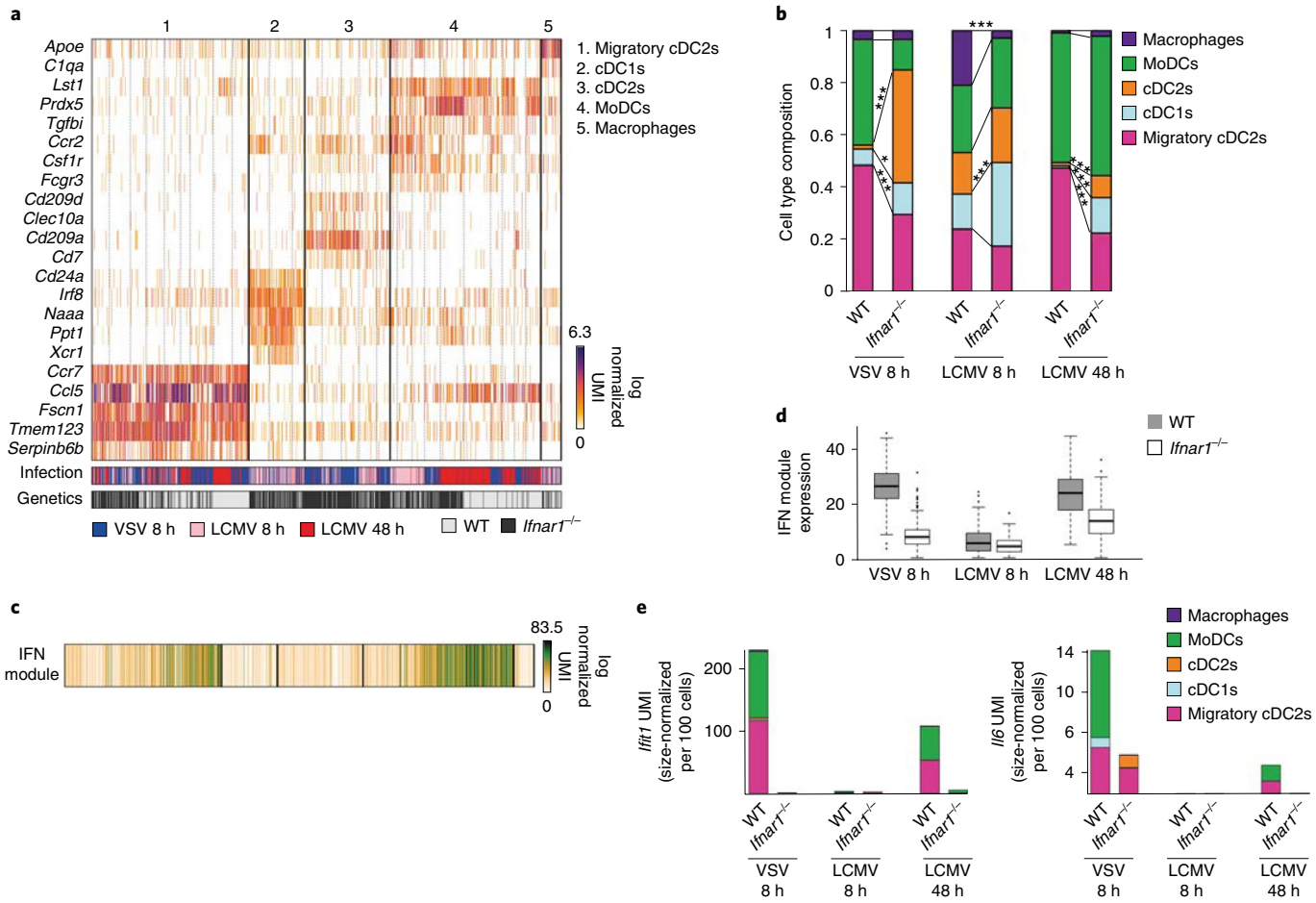

Fig. 5 | scRNA-seq analysis of LN DCs upon viral infection. a, Gene expression profiles of 2,179 single LN CD11c$^+$MHC-II^{hi} cells passing quality control grouped in five clusters. The color bars indicates each cell's origin (blue, cells from the popliteal LN of mice 8 h after intrafootpad rVSV infection; pink, cells from the popliteal LN of mice 8 h after intrafootpad rLCMV infection; red, cells from the popliteal LN of mice 48 h after intrafootpad rLCMV infection; light gray, wild-type mice; black, *Ifnar1*$^{-/-}$ mice). **b**, Relative abundance of different DC clusters 8 h after rVSV infection, 8 h after rLCMV infection and 48 h after rLCMV infection. Lines show differences in cluster abundance between wild-type and *Ifnar1*$^{-/-}$ mice under the same infection condition. Significant differences in abundance are highlighted. Two-sided FDR-adjusted Fisher's exact test: $^*P < 0.05$, $^{***}P < 0.001$. **c**, Color bar showing total size-normalized (by total number of UMIs in each cell) expression of ISGs in the cells in **a**. Detailed expression data for individual ISGs are shown in Extended Data Fig. 10. **d**, Distribution of total size-normalized expression of ISGs in CD11c$^+$MHC-II^{hi} cells grouped by experimental condition. **e**, Total expression of the ISG *Ifit1* and the T_{FH} cell-promoting cytokine *Il6* in different experimental conditions. Values represent size-normalized total transcripts per 100 cells. Colors represent relative contribution from the five different DC subsets.

studies have shown that type I IFN promoted T_{FH} cell differentiation, others reported that type I IFN suppressed the formation of T_{FH} cells or induced T_H1 cells[32]. Our results suggest that spatial and temporal regulation of type I IFN is critical for its effect on DCs, thus providing a potential explanation for the above-mentioned conflicting results. The cellular source of type I IFN in VSV and LCMV infections is an interesting question but, unfortunately, one that is technically difficult to address because of the many isoforms of type I IFN and the lack of a sensitive, robust type I IFN reporter mouse that would allow for unambiguous identification of cells producing small amounts of these cytokines[38,39]. VSV induces production of type I IFN in subcapsular sinus macrophages and plasmacytoid DCs[40]. However, the relative contribution of each LN cell type to the production of type I IFN after subcutaneous infection with LCMV or the recombinant viral strains used in this study is unknown[41]. Nevertheless, it is tempting to speculate that subcapsular sinus macrophages might be the critical cellular source of the early type I IFN response necessary for T_{FH} cell differentiation. Pertinent to this, it is worth noting that viral infections induce relocalization of subcapsular sinus macrophages to inner follicular areas and toward the anatomical niche where antiviral CD4$^+$ T cell priming takes place[42].

Our data identify DCs as the necessary platform that integrates early type I IFN signaling to promote T_{FH} cell differentiation. Mechanistically, type I IFN is necessary for induction of the T_{FH} cell-promoting cytokine IL-6 (ref. [35]). Our scRNA-seq data identified subsets of DCs (migratory cDC2s and moDCs) that produced *Il6* mRNA in response to early, but not late, type I IFN. One experimental caveat is that we analyzed DCs from the entire LN, rather than from the CD4$^+$ T cell priming niche, thus potentially underestimating the localized production of IL-6 by DCs. The relative contribution of DC-derived IL-6, as compared to IL-6 from other cellular sources, in shaping antiviral CD4$^+$ T cell polarization remains to be determined.

We found that CD4$^+$ T cells that differentiated into T_{FH} cells after rVSV infection showed relatively high velocity and a high meandering index, whereas CD4$^+$ T cells that differentiated into T_H1 cells after rLCMV infection were characterized by reduced mean speed and a lower meandering index. A mechanistic explanation

for these different motility behaviors remains elusive and might potentially include intrinsic differences in motility between T_{FH} and T_H1 cells, differences in spatial constraints provided by the different anatomical niches they occupy (B cell follicles versus interfollicular and T cell areas), different adhesion molecule expression and different antigen levels.

Blockade of early type I IFN signaling or of IL-6 resulted in reduced generation of T_{FH} cells and, consequently, reduced antiviral antibody responses. Of note, whereas the main effect of type I IFN blockade was observed on antiviral IgG1 titers, IL-6 blockade affected mostly the levels of antiviral IgG2b. The reason for this discrepancy is unknown but might lie with additional T cell-independent roles of IL-6 that affect B cell differentiation[43].

Although the data presented in this study link T_{FH} cell differentiation to early type I IFN sensing by DCs, they do not fully explain the strong T_H1 cell differentiation observed during LCMV infection. In addition to a lack of early type I IFN and IL-6, as reported here, LCMV might promote T_H1 cell differentiation through induction of T_H1 cell-polarizing cytokines, such as IL-12 and IFN-γ (refs. [44–46]). Although IL-12 is dispensable for T_H1 cell polarization upon LCMV infection[47,48], the role of other cytokines such as IFN-γ on antiviral $CD4^+$ T cell differentiation, their cellular source and their potential interference with IL-6 induction warrant further investigation.

In conclusion, we have characterized the cellular and molecular composition of the LN niches where $CD4^+$ T cell differentiation occurs, delineated the spatiotemporal dynamics of the ensuing helper T cell subsets and identified tight spatiotemporal regulation of type I IFN expression as a critical regulator of antiviral $CD4^+$ T cell polarization. Our model predicts that, if viruses induce an early wave of type I IFN (a situation that typically occurs with fast-replicating, highly cytopathic viruses that are controlled by neutralizing antibodies), this cytokine acts on migratory cDC2s and/or moDCs to induce IL-6 (and possibly other T_{FH} cell-promoting cytokines), drive T_{FH} cell differentiation and ultimately enhance humoral immunity; by contrast, if type I IFN is induced later upon viral infection (a situation that is typical of slow-replicating, non-cytopathic viruses that are controlled by the $CD8^+$ T cell response), DCs no longer make IL-6 and helper T cell polarization is biased toward non-T_{FH} cell fates such as T_H1 cells, which favor cellular immunity at the expense of B cell responses.

Online content

Any methods, additional references, Nature Research reporting summaries, source data, extended data, supplementary information, acknowledgements, peer review information; details of author contributions and competing interests; and statements of data and code availability are available at https://doi.org/10.1038/s41590-020-0596-6.

Received: 9 April 2019; Accepted: 10 January 2020;
Published online: 17 February 2020

References

1. Hale, J. S. et al. Distinct memory $CD4^+$ T cells with commitment to T follicular helper- and T helper 1-cell lineages are generated after acute viral infection. *Immunity* **38**, 805–817 (2013).
2. Wu, T. et al. Cutting edge: miR-17-92 is required for both CD4 Th1 and T follicular helper cell responses during viral infection. *J. Immunol.* **195**, 2515–2519 (2015).
3. Crotty, S. Follicular helper CD4 T cells (T_{FH}). *Annu. Rev. Immunol.* **29**, 621–663 (2011).
4. Vinuesa, C. G., Linterman, M. A., Yu, D. & MacLennan, I. C. Follicular helper T cells. *Annu. Rev. Immunol.* **34**, 335–368 (2016).
5. Szabo, S. J. et al. A novel transcription factor, T-bet, directs Th1 lineage commitment. *Cell* **100**, 655–669 (2000).
6. Arnaout, R. A. & Nowak, M. A. Competitive coexistence in antiviral immunity. *J. Theor. Biol.* **204**, 431–441 (2000).
7. Hangartner, L., Zinkernagel, R. M. & Hengartner, H. Antiviral antibody responses: the two extremes of a wide spectrum. *Nat. Rev. Immunol.* **6**, 231–243 (2006).
8. Kuka, M. & Iannacone, M. Viral subversion of B cell responses within secondary lymphoid organs. *Nat. Rev. Immunol.* **18**, 255–265 (2018).
9. Maloy, K. J. et al. Qualitative and quantitative requirements for $CD4^+$ T cell-mediated antiviral protection. *J. Immunol.* **162**, 2867–2874 (1999).
10. Oxenius, A., Bachmann, M. F., Zinkernagel, R. M. & Hengartner, H. Virus-specific MHC-class II-restricted TCR-transgenic mice: effects on humoral and cellular immune responses after viral infection. *Eur. J. Immunol.* **28**, 390–400 (1998).
11. Fazilleau, N., McHeyzer-Williams, L. J., Rosen, H. & McHeyzer-Williams, M. G. The function of follicular helper T cells is regulated by the strength of T cell antigen receptor binding. *Nat. Immunol.* **10**, 375–384 (2009).
12. Fallet, B. et al. Interferon-driven deletion of antiviral B cells at the onset of chronic infection. *Sci. Immunol.* **1**, eaah6817 (2016).
13. Osokine, I. et al. Type I interferon suppresses de novo virus-specific CD4 Th1 immunity during an established persistent viral infection. *Proc. Natl Acad. Sci. USA* **111**, 7409–7414 (2014).
14. Kerfoot, S. M. et al. Germinal center B cell and T follicular helper cell development initiates in the interfollicular zone. *Immunity* **34**, 947–960 (2011).
15. Mempel, T. R., Henrickson, S. E. & Von Andrian, U. H. T-cell priming by dendritic cells in lymph nodes occurs in three distinct phases. *Nature* **427**, 154–159 (2004).
16. Gerner, M. Y., Casey, K. A., Kastenmuller, W. & Germain, R. N. Dendritic cell and antigen dispersal landscapes regulate T cell immunity. *J. Exp. Med.* **214**, 3105–3122 (2017).
17. Groom, J. R. et al. CXCR3 chemokine receptor–ligand interactions in the lymph node optimize $CD4^+$ T helper 1 cell differentiation. *Immunity* **37**, 1091–1103 (2012).
18. Medaglia, C. et al. Spatial reconstruction of immune niches by combining photoactivatable reporters and scRNA-seq. *Science* **358**, 1622–1626 (2017).
19. Victora, G. D. et al. Germinal center dynamics revealed by multiphoton microscopy with a photoactivatable fluorescent reporter. *Cell* **143**, 592–605 (2010).
20. Hangartner, L. et al. Antiviral immune responses in gene-targeted mice expressing the immunoglobulin heavy chain of virus-neutralizing antibodies. *Proc. Natl Acad. Sci. USA* **100**, 12883–12888 (2003).
21. Cook, K. D., Kline, H. C. & Whitmire, J. K. NK cells inhibit humoral immunity by reducing the abundance of $CD4^+$ T follicular helper cells during a chronic virus infection. *J. Leukoc. Biol.* **98**, 153–162 (2015).
22. Narni-Mancinelli, E. et al. Fate mapping analysis of lymphoid cells expressing the NKp46 cell surface receptor. *Proc. Natl Acad. Sci. USA* **108**, 18324–18329 (2011).
23. Buch, T. et al. A Cre-inducible diphtheria toxin receptor mediates cell lineage ablation after toxin administration. *Nat. Methods* **2**, 419–426 (2005).
24. Odermatt, B., Eppler, M., Leist, T. P., Hengartner, H. & Zinkernagel, R. M. Virus-triggered acquired immunodeficiency by cytotoxic T-cell-dependent destruction of antigen-presenting cells and lymph follicle structure. *Proc. Natl Acad. Sci. USA* **88**, 8252–8256 (1991).
25. Borrow, P., Evans, C. F. & Oldstone, M. B. Virus-induced immunosuppression: immune system-mediated destruction of virus-infected dendritic cells results in generalized immune suppression. *J. Virol.* **69**, 1059–1070 (1995).
26. Moseman, E. A., Wu, T., de la Torre, J. C., Schwartzberg, P. L. & McGavern, D. B. Type I interferon suppresses virus-specific B cell responses by modulating $CD8^+$ T cell differentiation. *Sci. Immunol.* **1**, eaah3565 (2016).
27. Isogawa, M., Chung, J., Murata, Y., Kakimi, K. & Chisari, F. V. CD40 activation rescues antiviral $CD8^+$ T cells from PD-1-mediated exhaustion. *PLoS Pathog.* **9**, e1003490 (2013).
28. Sammicheli, S. et al. Inflammatory monocytes hinder antiviral B cell responses. *Sci. Immunol.* **1**, eaah6789 (2016).
29. Boring, L. et al. Impaired monocyte migration and reduced type 1 (Th1) cytokine responses in C-C chemokine receptor 2 knockout mice. *J. Clin. Invest.* **100**, 2552–2561 (1997).
30. Eisenbarth, S. C. Dendritic cell subsets in T cell programming: location dictates function. *Nat. Rev. Immunol.* **19**, 89–103 (2018).
31. Li, J., Lu, E., Yi, T. & Cyster, J. G. EBI2 augments Tfh cell fate by promoting interaction with IL-2-quenching dendritic cells. *Nature* **533**, 110–114 (2016).
32. Kuka, M., De Giovanni, M. & Iannacone, M. The role of type I interferons in $CD4^+$ T cell differentiation. *Immunol. Lett.* **215**, 19–23 (2019).
33. Nurieva, R. I. et al. Generation of T follicular helper cells is mediated by interleukin-21 but independent of T helper 1, 2, or 17 cell lineages. *Immunity* **29**, 138–149 (2008).
34. Eto, D. et al. IL-21 and IL-6 are critical for different aspects of B cell immunity and redundantly induce optimal follicular helper CD4 T cell (Tfh) differentiation. *PLoS One* **6**, e17739 (2011).

35. Cucak, H., Yrlid, U., Reizis, B., Kalinke, U. & Johansson-Lindbom, B. Type I interferon signalling in dendritic cells stimulates the development of lymph-node-resident T follicular helper cells. *Immunity* **31**, 491–501 (2009).
36. Baran, Y. et al. MetaCell: analysis of single-cell RNA-seq data using *K*-nn graph partitions. *Genome Biol.* **20**, 206 (2019).
37. Chakarov, S. & Fazilleau, N. Monocyte-derived dendritic cells promote T follicular helper cell differentiation. *EMBO Mol. Med.* **6**, 590–603 (2014).
38. Scheu, S., Dresing, P. & Locksley, R. M. Visualization of IFNβ production by plasmacytoid versus conventional dendritic cells under specific stimulation conditions in vivo. *Proc. Natl Acad. Sci. USA* **105**, 20416–20421 (2008).
39. Kumagai, Y. et al. Alveolar macrophages are the primary interferon-α producer in pulmonary infection with RNA viruses. *Immunity* **27**, 240–252 (2007).
40. Iannacone, M. et al. Subcapsular sinus macrophages prevent CNS invasion on peripheral infection with a neurotropic virus. *Nature* **465**, 1079–1083 (2010).
41. Trinchieri, G. Lymphocyte choriomeningitis virus plays hide-and-seek with type 1 interferon. *Cell Host Microbe* **11**, 553–555 (2012).
42. Gaya, M. et al. Inflammation-induced disruption of SCS macrophages impairs B cell responses to secondary infection. *Science* **347**, 667–672 (2015).
43. Kawano, Y., Noma, T., Kou, K., Yoshizawa, I. & Yata, J. Regulation of human IgG subclass production by cytokines: human IgG subclass production enhanced differentially by interleukin-6. *Immunology* **84**, 278–284 (1995).
44. Hsieh, C. S. et al. Development of T_H1 $CD4^+$ T cells through IL-12 produced by *Listeria*-induced macrophages. *Science* **260**, 547–549 (1993).
45. Bradley, L. M., Dalton, D. K. & Croft, M. A direct role for IFN-γ in regulation of Th1 cell development. *J. Immunol.* **157**, 1350–1358 (1996).
46. Heufler, C. et al. Interleukin-12 is produced by dendritic cells and mediates T helper 1 development as well as interferon-γ production by T helper 1 cells. *Eur. J. Immunol.* **26**, 659–668 (1996).
47. Oxenius, A., Karrer, U., Zinkernagel, R. M. & Hengartner, H. IL-12 is not required for induction of type 1 cytokine responses in viral infections. *J. Immunol.* **162**, 965–973 (1999).
48. Schijns, V. E. et al. Mice lacking IL-12 develop polarized Th1 cells during viral infection. *J. Immunol.* **160**, 3958–3964 (1998).

Methods

Mice. C57BL/6, CD45.1 (inbred C57BL/6), *Actb*-CFP (B6.129(ICR)-Tg(CAG-ECFP) CK6Nagy/J), *Actb*-GFP (C57BL/6-Tg(CAG-EGFP)1Osb/J), *Ccr2*$^{-/-}$ (B6.129S4-Ccr2tm1Ifc/J), *Rosa26*-ZsGreen (B6.Cg-Gt(ROSA)26Sor$^{tm6(CAG-ZsGreen1)Hze}$/J)[49] and PA-GFP[19] mice were purchased from Charles River or the Jackson Laboratory. LCMV-P14 (ref. [50]), SMARTA[10], Tg7 (ref. [9]) and *Ifnar1*$^{-/-}$ (ref. [51]) mice were obtained through the Swiss Immunological Mouse Repository (SwImMR). Transgenic mice expressing the heavy and light chain of a BCR specific for VSV Ind (VI10YEN[20]) were obtained through the European Virus Archive. Mice transgenic for a BCR specific for LCMV WE (KL25) bred to *Actb*-DsRed mice were described previously[28]. Cor93 TCR-transgenic mice (lineage BC10.3, inbred CD45.1), in which >98% of splenic CD8$^+$ T cells recognize a Kb-restricted epitope located between residues 93–100 in the hepatitis B virus core protein (MGLKFRQL), have been described previously[27]. *Xcr1*-DTR–Venus, *Cd11c*-Cre and *Ifnar1*$^{fl/fl}$ mice have also been described previously[52–54]. *Ncr1*-Cre[22] mice were obtained from E. Vivier (Centre d'Immunologie de Marseille-Luminy). *Rosa26*-iDTR[23] mice were obtained from M. Bacigaluppi (San Raffaele Scientific Institute). *Cx3cr1*$^{GFP/+}$ (ref. [55]) and *Ccr2*$^{RFP/+}$ (ref. [56]) mice were provided by I. Charo (University of California, San Francisco) by way of B. Engelhardt (University of Bern). Bone marrow chimeras were generated by irradiation of C57BL/6 mice with ~900 rad and reconstitution with the indicated bone marrow; mice were allowed to reconstitute for at least 8 weeks before use. Mice were housed under specific-pathogen-free conditions and used at 8–10 weeks of age, unless otherwise indicated. In all experiments, mice were matched for age and sex before experimental manipulation. All experimental animal procedures were approved by the Institutional Animal Committee of the San Raffaele Scientific Institute.

Infections and immunizations. Unless otherwise indicated, mice were infected via the footpad with 1×10^5 p.f.u. of VSV serotype Ind, VSV serotype New Jersey or rVSV (a recombinant VSV expressing an LCMV GP recognized by both SMARTA TCR-transgenic and KL25 BCR-transgenic cells instead of the VSV GP) or with 1×10^5 f.f.u. of LCMV Armstrong, LCMV WE, LCMV clone 13 or rLCMV (a recombinant LCMV clone 13 expressing an LCMV GP recognized by both SMARTA TCR-transgenic and KL25 BCR-transgenic cells instead of the LCMV Cl13 GP)[12,28].

In indicated experiments, mice were infected with 1×10^2, 1×10^5 or 1×10^7 p.f.u. of VSV Ind or 1×10^2, 1×10^5 or 1×10^7 f.f.u. of LCMV WE. In indicated experiments, mice were infected intravenously with 1×10^6 f.f.u. of LCMV Armstrong or LCMV clone 13 or with 1×10^6 p.f.u. of VSV Ind. Viruses were propagated and quantified as described[12,28] and were diluted in 25 µl of PBS before footpad injection or in 200 µl of PBS before intravenous injection.

Mice were retro-orbitally bled at the indicated time points for GP-specific antibodies measured by GP-1-binding ELISA[57]. Anti-mouse IgG1 and IgG2b from the SBA Clonotyping System-C57BL/6-HRP kit (Southern Biotech) were used at a 1:1,000 dilution to detect GP-binding antibodies.

All infectious work was performed in designated Biosafety Level 2 (BSL-2) and BSL-3 workspaces in accordance with institutional guidelines.

T and B cell isolation, adoptive transfer and in vivo treatments. Naive CD4$^+$ T cells from the spleens of SMARTA CD45.1$^+$, SMARTA GFP$^+$, SMARTA CFP$^+$ and SMARTA *Ifnar1*$^{-/-}$ transgenic mice, CD8$^+$ T cells from the spleens of LCMV-P14-GFP mice and naive B cells from the spleens of wild-type and KL25-DsRed mice were negatively selected by magnetic isolation (Miltenyi Biotec), with purity always above 98% as determined by flow cytometry. Unless otherwise indicated, 1×10^6 SMARTA CD45.1$^+$ T cells were injected intravenously into indicated recipients 1 d before intrafootpad infection. In all imaging experiments, 3×10^7 purified naive B cells were labeled with 1 µM Deep Red (Life Technologies) for 20 min at 37 °C in RPMI before adoptive transfer. In selected imaging experiments (12 and 48 h after infection), 1×10^7 or 5×10^6 SMARTA GFP$^+$ or CFP$^+$, 5×10^6 P14 GFP$^+$ and 5×10^6 KL25 DsRed$^+$ cells were injected. In indicated experiments, mice were treated with InVivoMab anti-IFNAR (MAR-15A3, BioXcell; 1 mg intravenously 1 d before or 1 d after infection) or mouse IgG1 isotype control (MOPC-21, BioXcell); anti-IL-6 (MP5-20F3, BioXcell; 0.5 mg intravenously 1 d before or 1 d after infection and 0.25 mg every other day) or rat IgG1 isotype control (BioXcell); InVivoMab anti-ICOS (7E.17G9, BioXcell; 0.5 mg intravenously 2 and 1 d before infection) or rat IgG2b isotype control (LTF-2, BioXcell); or 25 µg of poly(I:C) HMW (InvivoGen; intrafootpad injection the day of the infection and 1 d after). To deplete cDC1s and NK cells, 500 ng of diphtheria toxin (Millipore) diluted in 200 µl of PBS was administered intraperitoneally 1 d before the infection and every other day thereafter to *Xcr1*-DTR and *Ncr1*-DTR mice, respectively.

Cell isolation and flow cytometry. Single-cell suspensions of spleens and LNs were generated as described[28,58]. All flow cytometry staining of surface-expressed and intracellular molecules was performed as described[28]. Antibodies used recognized the following molecules: Bcl-6 (K112-91), T-bet (4B10), CXCR5 (2G8), CD4 (RM4-5), CD45.1 (A20), CD45.2 (K104), CD44 (IM7), IgD (11-26C.2A), NK1.1 (PK136), TCRβ (H57-597), CD8 (K53-6.7), CD11c (N418), CD11b (M1/70), MHC-II (AF6-120.1), IgG1 (A85-1), CD95 (JO2), B220 (RA3-6B2), CD69 (H1.2F3) and CD25 (PC61). Fluorochrome-conjugated antibodies were purchased from BioLegend, eBioscience or BD Pharmingen. All flow cytometry analyses were performed in FACS buffer containing PBS with 2 mM EDTA and 2% FBS on a FACS CANTO (BD Pharmingen), and data were analyzed with FlowJo software (Treestar).

Confocal immunofluorescence histology. Confocal microscopy analysis of popliteal LNs was performed as previously described[28]. The following antibodies were used for staining: rat anti-B220 (RA3-6B2) and rabbit anti-GFP (Invitrogen). Images were acquired on an inverted Leica microscope (SP8, Leica Microsystems) with a motorized stage for tiled imaging using an HC PL APO CS2 ×20 objective (NA 0.75). To minimize fluorophore spectral spillover, we used the Leica sequential laser excitation and detection modality. B cell follicles were defined on the basis of the position of polyclonal B cells or B220 staining. For three-dimensional image acquisition, ten *xy* stacks (1,024×1,024 pixels) sampled with 2-µm *z* spacing were acquired to provide image volumes that were 20 µm in depth.

Confocal imaging analysis. Antigen-specific CD4$^+$ T cells were localized with the Imaris built-in spot detection function, and follicular T cells were identified on the basis of polyclonal B cell position. The center of the T cell area was geometrically identified in Imaris 9.0.2 (Bitplane). Distances from the center of the T cell area were calculated and normalized for the volume of the T cell area. A T cell cluster was defined as a minimum of three T cells within a distance of 15 µm measured from the centroid of each cell, as previously reported[59]. Spot-to-spot closest distance was calculated to detect 'clustered' spots (spot-to-spot closest distance ≤ 15 µm). Cell clusters of fewer than three cells were manually removed.

Intravital multiphoton microscopy. Mice were anesthetized with 5% isoflurane (Abbot) through a nose cone also delivering oxygen at 1 liter min^{-1}. Follow-up surgery and popliteal LN intravital imaging were carried out with lower concentrations of isoflurane (between 0.5% and 0.8%, adjusted according to breathing rate). Surgical preparation of the popliteal LN was performed as described[28,60]. Images were acquired with a LaVision BioTec TriMScope II coupled to an Olympus BX51 upright microscope enclosed in a custom-built environmental chamber (Life Imaging Services) that was maintained at 37 °C with heated air. Continuous body temperature monitoring through a rectal probe was performed to ensure that a narrow range of 37–38 °C was maintained at all times. Fluorescence excitation was provided by two tunable fs-pulsed Ti:Sa lasers (680–1,080 nm, Ultra II, Coherent) and an optical parameter oscillator (1,000–1,600 nm, APE Chameleon OPO, Coherent). The setup included four photomultiplier tubes (three Hamamatsu H7422-40 GaAsP High-Sensitivity PMTs and one Hamamatsu H7422-50 GaAsP High-Sensitivity red-extended PMT) with four emission filters (BS495, ET525/50, ET595/40 and BS624) and a high-working-distance water-immersion ×25 objective (NA 1.05, Olympus) or ×20 objective (NA 1.0, Zeiss). For four-dimensional analysis of cell migration, stacks of ten square *xy* sections (512×512 pixels) sampled with 5-µm *z* spacing were acquired every 10 s for up to 1.5 h to provide image volumes that were 50 µm in depth and had an *xy* field of view variable between 356×356 µm^2 and 409×409 µm^2. Sequences of image stacks were transformed into volume-rendered four-dimensional time-lapse movies with Imaris 9.0.2 (Bitplane). The mean track speed and meandering index (the ratio of a migrating cell's linear displacement to the total path length) were calculated by a semiautomated cell tracking algorithm from Imaris.

Intravital cytometry. Intravital cytometry was performed by adapting a method for histocytometry[61]. Briefly, T and B cell surfaces were created by the surface object creation wizard in Imaris 9.0.2 (Bitplane). T and B cell surfaces were then merged into T–B surfaces with the merge function in Imaris. Channel statistics from T–B merged surfaces were exported and merged into combined CSV files (Python) that were uploaded and analyzed on FlowJo X[61].

NICHE-seq. NICHE-seq was performed as previously described[18]. Briefly, an Olympus BX51 upright microscope fitted with tunable fs-pulsed Ti:Sa lasers was used to photoactivate and image niches of interest (680–1,080 nm, Ultra II, Coherent). Images were acquired with a two-photon laser tuned to 940 nm. Regions within the outer paracortex of dLNs (with antigen-specific CD4$^+$ T cell clusters) were photoactivated at 820 nm (ref. [19]). Tile images were acquired as 20- to 30-µm *z* stacks with 5-µm steps between each *z* plane. Images were acquired at 512×512 *xy* resolution. The volume and depth along the *z* axis of the photoactivated zones were consistent among experiments.

Immediately after photoactivation, LNs were forced through 70-µm mesh into ice-cold FACS buffer (2 mM EDTA (pH 8.0), 0.5% BSA in PBS). Cell populations were sorted with a BD FACSAria fusion (BD Biosciences). Because in individual photoactivated cells only a fraction of the inactive PA-GFP is converted to active PA-GFP, photoactivated PA-GFP cells express both activated PA-GFP (detectable upon excitation at 488 nm) and inactive PA-GFP (detectable upon excitation at 405 nm) by flow cytometry. After exclusion of doublets, isolated cells underwent single-cell sorting into 384-well cell capture plates containing 2 µl of lysis solution and barcoded poly(T) reverse transcription primers for scRNA-seq. Four empty wells were kept in each 384-well plate as a no-cell control during data analysis. Immediately after sorting, each plate was spun down to ensure cell immersion in the lysis solution, snap frozen on dry ice and stored at −80 °C until processing.

Single-cell RNA sequencing. DCs were sorted with a BD FACSAria fusion (BD Biosciences). After exclusion of doublets, cells positive for CD11c and MHC-II but negative for CD3 and B220 underwent single-cell sorting into 384-well cell capture plates containing 2 µl of lysis solution and barcoded poly(T) reverse transcription primers for scRNA-seq. Immediately after sorting, each plate was

spun down to ensure cell immersion in the lysis solution, snap frozen on dry ice and stored at −80 °C until processing.

Massively parallel single-cell RNA sequencing library preparation. Single-cell libraries were prepared as previously described[62]. Briefly, mRNA from cells sorted into cell capture plates was barcoded, converted to cDNA and pooled with an automated pipeline. The pooled sample was then linearly amplified by T7 in vitro transcription, and the resulting RNA was fragmented and converted to a sequencing-ready library by tagging the samples with pool barcodes and Illumina sequences during ligation, reverse transcription and PCR. Each pool of cells was tested for library quality, and the concentration was assessed as described[62].

All RNA-seq libraries (pooled at equimolar concentrations) were sequenced on the Illumina NextSeq 500 platform at a median sequencing depth of 38,323 reads per cell. Sequences were mapped to the mouse genome (mm9), demultiplexed and filtered as described[62], extracting a set of unique molecular identifiers that defined distinct transcripts in single cells for further processing. We estimated the level of spurious UMIs in the data with statistics on empty MARS-seq wells and excluded all plates with estimated noise of >5%. Mapping of reads was done with HISAT (v0.1.6); reads with multiple mapping positions were excluded. Reads were associated with genes if they were mapped to an exon, using the UCSC Genome Browser for reference. Exons of different genes that shared a genomic position on the same strand were considered to represent a single gene with a concatenated gene symbol. Cells with fewer than 500 UMIs were discarded from the analysis.

Clustering of infected lymph nodes. For clustering of scRNA-seq data from infected LNs, we used the R package MetaCell[36]. MetaCell was used to derive informative genes and compute cell-to-cell similarity, to compute *K*-nn graph covers and derive the distribution of RNA in cohesive groups of cells (or meta-cells), and to derive strongly separated clusters by bootstrap analysis and computation of graph covers on resampled data. Default parameters were used unless otherwise stated. Cells from rVSV- and rLCMV-infected LNs were clustered together. Meta-cells were annotated by pooled differential expression of marker genes, using the $FP_{gene,mc}$ metric, which signifies for each gene and meta-cell the fold change between the geometric mean of the gene within the meta-cell and the median geometric mean across all meta-cells. Each gene was given an FP threshold and a priority index, such that coloring for activated T cells by *Gzma* was favored over coloring for general T cells by *Trbc2*. The selected genes, priorities and fold change threshold parameters were as follows:

Group	Gene	Priority	Fold change
T	*Trbc2*	1	2
T	*Cd3e*	1	2
CD8T	*Cd8a*	2	2.5
NK	*Klrb1c*	3	2
ActT	*Gzma*	4	2
Unknown	*Gm23935*	3	2
CD4T	*Cd4*	3	1.5
DC	*Cxcl16*	5	2
Mono	*Fcer1g*	2	3
B	*Cd79b*	3	0.6

Clustering of dendritic cells. For clustering of scRNA-seq data from $CD11c^{+}MHC\text{-}II^{hi}$ DCs, we used the R package MetaCell[36], as previously described. Cells from rVSV- and rLCMV-infected LNs, from all time points and genetic backgrounds, were clustered. Meta-cells were annotated by pooled differential expression of marker genes, as described above. The selected genes, priorities and fold change threshold parameters were as follows:

Group	Gene	Priority	Fold change
Migratory cDC2	*Fscn1*	1	5
Migratory cDC2	*Il12b*	1	2
cDC1	*Naaa*	1	3
cDC1	*Cd24a*	1	2.5
cDC2	*Cd209a*	2	5
cDC2	*Cd209d*	2	1.8
MoDC	*Csf1r*	4	3
MoDC	*Tgfbi*	4	2
MoDC	*Fcer1g*	4	2
Macrophage	*C1qb*	5	4

qPCR. Total RNA was isolated from frozen LNs with the ReliaPrep RNA Miniprep system (Promega), following the manufacturer's instructions. One microgram of total RNA was reverse transcribed before qPCR analyses for *Ifna2* (Mm00833961_S1), *Ifna4* (Mm00833969_S1), *Ifna5* (Mm00833976_S1), *Ifna6* (Mm01703458_S1), *Ifna7* (Mm02525960_S1), *Ifna9* (Mm00833983_S1), *Ifna12* (Mm00616656_S1), *Ifna13* (Mm01731013_S1), *Ifna14* (Mm01703465_S1), *Ifnb* (Mm00439552_S1), *Isg15* (Mm 01705338_S1), *Oas2* (Mm00460961_m1) and *Il6* (Mm00446190_M1) in a QuantStudio 5 Real-Time PCR System (all from Thermo Fisher Scientific). All experiments were done in duplicate, and data were normalized to the housekeeping gene *Gapdh* (Mm99999915_g1, Thermo Fisher Scientific).

Statistical analyses. Results are expressed as the mean ± s.e.m. All statistical analyses were performed in Prism 5 (GraphPad Software). Means between two groups were compared with unpaired two-tailed *t* tests. Means among three or more groups were compared with one-way or two-way ANOVA. The Bonferroni post test was used to correct for multiple comparisons, and in some experiments Fisher's LSD post test was used when correction for multiple comparisons was not necessary.

Reporting Summary. Further information on research design is available in the Nature Research Reporting Summary linked to this article.

Data availability

All data are available in the main text or the Supplementary Information. RNA-seq data that support the findings of this study have been deposited in the Gene Expression Omnibus (GEO) under accession GSE130009. Source data for Figs. 1–4 and Extended Data Figs. 1, 2, 5–7 and 9 are presented with the paper.

References

49. Madisen, L. et al. A robust and high-throughput Cre reporting and characterization system for the whole mouse brain. *Nat. Neurosci.* **13**, 133–140 (2010).
50. Pircher, H., Bürki, K., Lang, R., Hengartner, H. & Zinkernagel, R. M. Tolerance induction in double specific T-cell receptor transgenic mice varies with antigen. *Nature* **342**, 559–561 (1989).
51. Müller, U. et al. Functional role of type I and type II interferons in antiviral defense. *Science* **264**, 1918–1921 (1994).
52. Yamazaki, C. et al. Critical roles of a dendritic cell subset expressing a chemokine receptor, XCR1. *J. Immunol.* **190**, 6071–6082 (2013).
53. Caton, M. L., Smith-Raska, M. R. & Reizis, B. Notch–RBP-J signalling controls the homeostasis of $CD8^{-}$ dendritic cells in the spleen. *J. Exp. Med.* **204**, 1653–1664 (2007).
54. Prigge, J. R. et al. Type I IFNs act upon hematopoietic progenitors to protect and maintain hematopoiesis during *Pneumocystis* lung infection in mice. *J. Immunol.* **195**, 5347–5357 (2015).
55. Jung, S. et al. Analysis of fractalkine receptor CX_3CR1 function by targeted deletion and green fluorescent protein reporter gene insertion. *Mol. Cell. Biol.* **20**, 4106–4114 (2000).
56. Saederup, N. et al. Selective chemokine receptor usage by central nervous system myeloid cells in CCR2-red fluorescent protein knock-in mice. *PLoS One* **5**, e13693 (2010).
57. Eschli, B. et al. Early antibodies specific for the neutralizing epitope on the receptor binding subunit of the lymphocytic choriomeningitis virus glycoprotein fail to neutralize the virus. *J. Virol.* **81**, 11650–11657 (2007).
58. Tonti, E. et al. Bisphosphonates target B cells to enhance humoral immune responses. *Cell Rep.* **5**, 323–330 (2013).
59. Hor, J. L. et al. Spatiotemporally distinct interactions with dendritic cell subsets facilitates $CD4^{+}$ and $CD8^{+}$ T cell activation to localized viral infection. *Immunity* **43**, 554–565 (2015).
60. Sammicheli, S., Kuka, M. & Iannacone, M. Intravital imaging of B cell responses in lymph nodes. *Methods Mol. Biol.* **1763**, 63–74 (2018).
61. Tan, Y. et al. Streamlining volumetric multi-channel image cytometry using hue-saturation-brightness-based surface creation. *Commun. Biol.* **1**, 136 (2018).
62. Jaitin, D. A. et al. Massively parallel single-cell RNA-seq for marker-free decomposition of tissues into cell types. *Science* **343**, 776–779 (2014).

Acknowledgements

We thank M. Mainetti and M. Freschi for technical support; M. Silva for secretarial assistance; J.C. de la Torre (The Scripps Research Institute) for providing rLCMV; D. Pinschewer (University of Basel) for providing rVSV; M. Linterman (Babraham Institute) for providing *Cd11c*-Cre; $Ifnar1^{fl/fl}$ bone marrow; R. Pardi and A. Mondino for critical reading of the manuscript; and the members of the Iannacone laboratory for helpful discussions. Confocal immunofluorescence histology was carried out at Alembic, San Raffaele Scientific Institute, and the Vita-Salute San Raffaele University. Flow cytometry was carried out at FRACTAL, San Raffaele Scientific Institute. We would like to acknowledge the PhD program in Basic and Applied Immunology and Oncology

at Vita-Salute San Raffaele University, as V.C. and E.S. conducted this study as partial fulfillment of their PhD in Molecular Medicine within this program. M.I. is supported by European Research Council (ERC) Consolidator grant 725038, Italian Association for Cancer Research (AIRC) grants 19891 and 22737, Italian Ministry of Health (MoH) grant GR-2011-02347925, Lombardy Foundation for Biomedical Research (FRRB) grant 2015-0010, the European Molecular Biology Organization Young Investigator Program and a Career Development award from the Giovanni Armenise-Harvard Foundation. M.K. is supported by Italian Ministry of Education grants SIR-RBSI14BAO5 and PRIN-2017ZXT5WR.

Author contributions

M.D.G., V.C. and M.K. designed and performed experiments, analyzed data, performed the statistical analyses and drafted the manuscript. E.S., C.G.M., P.D.L., E.B., C.C., E.C., L.G. and A.F. performed experiments and analyzed data. A.G., C.M. and I.A. performed the NICHE-seq and scRNA-seq analyses and prepared the related figures. S.E. and W.K. performed the *Xcr1*-DTR experiments and analyzed data. M.K. provided funding, conceptual advice and supervision. M.I. designed and coordinated the study, provided funding and wrote the manuscript.

Competing interests

The authors declare no competing interests.

Additional information

Extended data is available for this paper at https://doi.org/10.1038/s41590-020-0596-6.

Supplementary information is available for this paper at https://doi.org/10.1038/s41590-020-0596-6.

Correspondence and requests for materials should be addressed to M.K. or M.I.

Peer review information Ioana Visan was the primary editor on this article and managed its editorial process and peer review in collaboration with the rest of the editorial team.

Reprints and permissions information is available at www.nature.com/reprints.

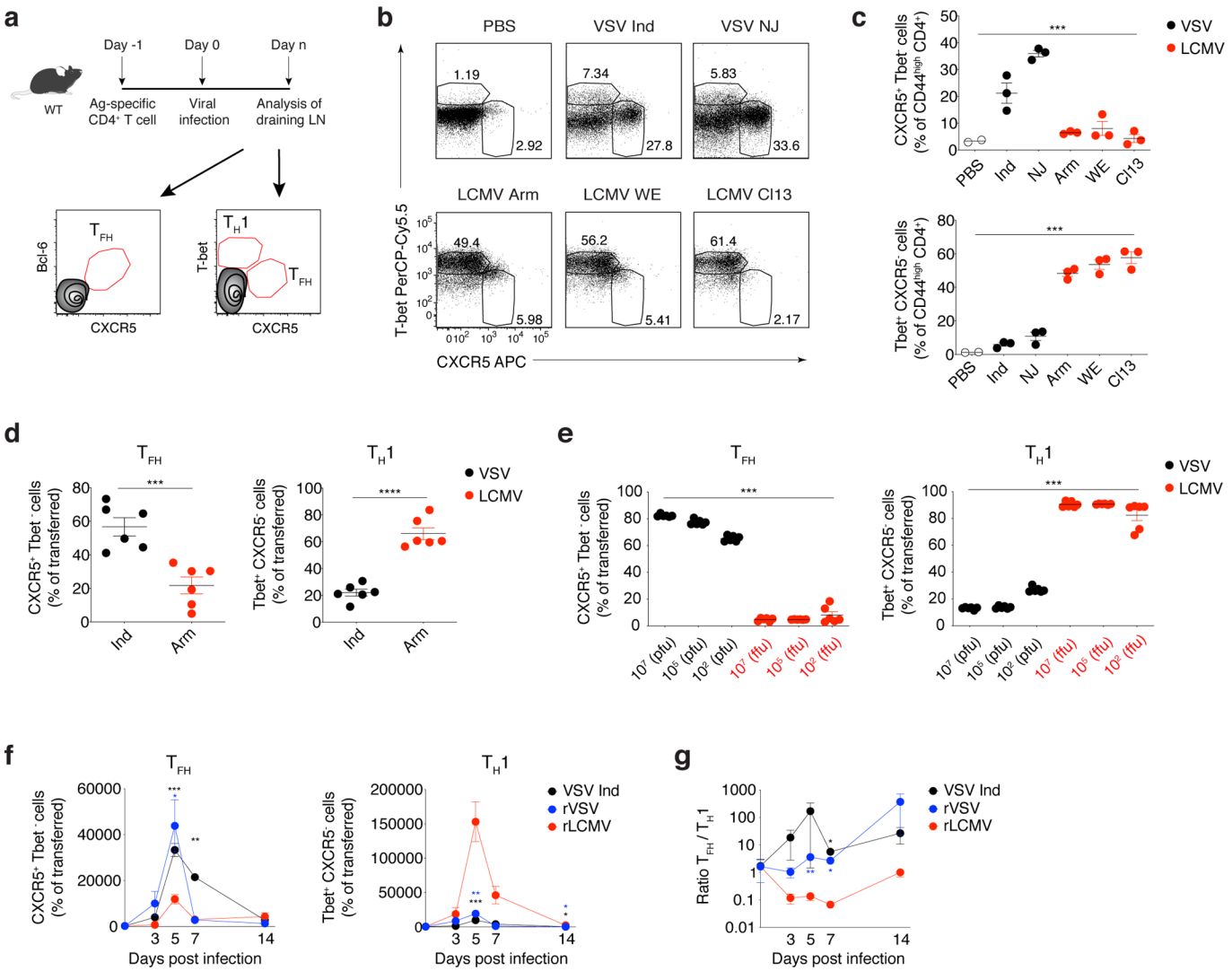

Extended Data Fig. 1 | VSV and LCMV infections result in distinct antiviral CD4⁺ T cell polarization and in vivo dynamic behavior, independently of viral strain, viral dose, infection route and TCR signal strength. a, Schematic representation of experimental procedure for the results described in Fig. 1a–c. 1×10^6 purified Ag-specific (Tg7 when VSV-Ind was used, SMARTA cells in all other cases) CD45.1⁺ CD4⁺ T cells were injected into CD45.2⁺ WT recipients 1 day before intrafootpad infection. dLNs were collected at the indicated time points after infection and analyzed by flow cytometry. T_{FH} were defined as either Bcl-6⁺ CXCR5⁺ or CXCR5⁺ T-bet⁻ cells (in the latter case we always verified that cells were also Bcl-6⁺); T_H1 were defined as T-bet⁺ CXCR5⁻ cells. **b**, Representative flow cytometry plots showing T_{FH} and T_H1 cells (out of CD44^{high} endogenous CD4⁺ T cells) in dLNs 7 days after footpad infection with the indicated virus. Numbers indicated the percentage of cells within the indicated gate. Results are representative of at least 2 independent experiments. **c**, Quantification of T_{FH} (top) and T_H1 cells (bottom)—expressed as percentages of CD44^{high} endogenous CD4⁺ T cells—in dLNs of mice described in **b**. Results are representative of at least 2 independent experiments. Mean± SEM is shown. PBS $n=2$, all other conditions $n=3$. A one-way Anova test was applied; *** *p value* < *0.001*. **d**, Quantification of T_{FH} (left) and T_H1 (right) cells (expressed as percentages out of total transferred cells) in the spleens of CD45.2⁺ WT recipients injected with 1×10^6 Ag-specific (Tg7 when VSV-Ind was used, SMARTA in all other cases) CD45.1⁺ T cells one day prior to intravenous infection with VSV-Ind (left), LCMV-Arm (right) or LCMV-Cl13 (not shown), respectively. Mean +/- SEM is shown. An unpaired two-tailed t test was applied. *** *p value* < *0.001*. **e**, Quantification of T_{FH} (left) and T_H1 (right) cells (expressed as percentages out of total transferred cells) in dLNs 5 days after infection of CD45.2⁺ WT recipients injected with 1×10^6 Ag-specific (Tg7 for VSV-Ind, SMARTA for LCMV-WE) CD45.1⁺ T cells one day prior to intrafootpad infection with the indicated doses of VSV-Ind (black) or LCMV-WE (red). Results are pooled from 2 independent experiments. Mean +/- SEM is shown.$n=6$. A one-way Anova test was applied. *** *p value* < *0.001*. **f-g**, Quantification of T_{FH} (left) and T_H1 (right) cell absolute numbers (**f**) or T_{FH}/T_H1 absolute number ratios (**g**) at 0,3,5,7 and 14 days after VSV-Ind (black), rVSV (blue) or rLCMV (red) infection. Mean +/- SEM is shown. Day 0 $n=3$ (VSV), 4 (rVSV and rLCMV); Day 3 $n=5$ (VSV), 7 (rVSV and rLCMV); Day 5 $n=5$ (VSV), 9 (rVSV), 10 (rLCMV); Day 7 $n=3$; Day 14 $n=3$ (VSV and rVSV), 6 (rLCMV). Black and blue stars indicate significance of respectively VSV and rVSV samples towards LCMV samples. A two-way Anova with LSD post-test was applied. * *p value* < *0.05*; ** *p value* < *0.01*; *** *p value* < *0.001*; **** *p value* < *0.0001*.

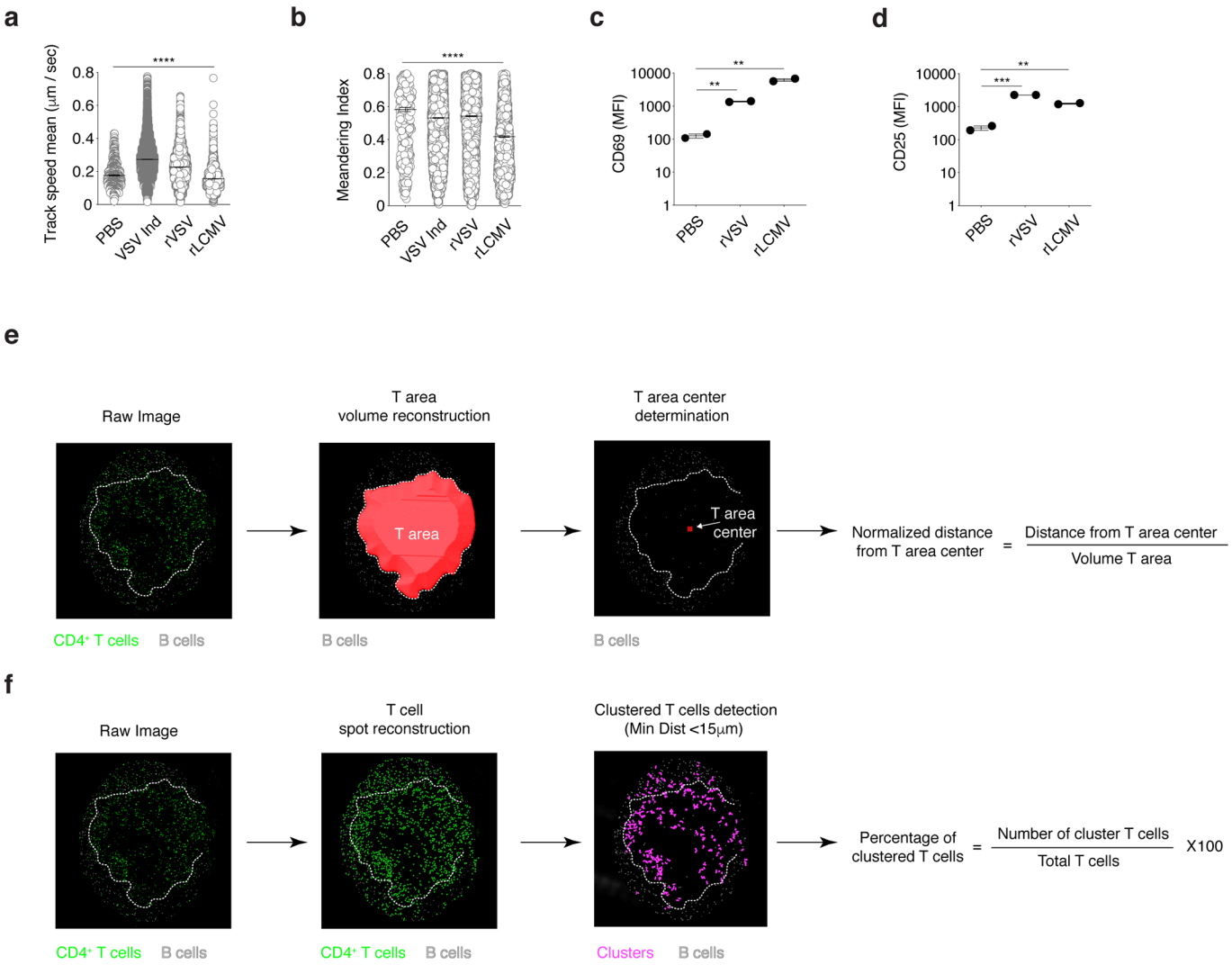

Extended Data Fig. 2 | Spatiotemporal dynamics and activation of Ag-specific CD4⁺ T cells within dLNs upon VSV or LCMV infection. (**a, b**) Track speed mean (**a**) and meandering index (**b**) of GFP⁺ Ag-specific (Tg7 when VSV-Ind was used, SMARTA in all other cases) CD4⁺ T cells in the mice described in Fig. 1d–g and Supplementary Movie 1, 3 days after PBS, VSV-Ind, rVSV or rLCMV injection. Data are pooled from 2 independent experiments. PBS, $n = 395$; VSV-Ind $n = 11219$; rVSV $n = 6692$; rLCMV $n = 3537$. One-way Anova test was applied. **** *p value* < *0.0001;* (**c, d**) Mean fluorescent intensity of CD69 (**c**) and CD25 (**d**) within Ag-specific (SMARTA) CD4⁺ T cells in dLNs, 2 days after PBS, rVSV or rLCMV injection. Data are representative of 2 independent experiments. Mean +/- SEM is shown. $n = 2$. One-way Anova test was applied. ** *p value* < *0.01;* *** *p value* < *0.001* (**e, f**) Methods used to determine the normalized distance from T area centre (**e**) and percentages of clustered T cells / section (**f**). **e**, T cell area volume was defined based on polyclonal B cell positioning and its centre was geometrically identified in Imaris. Ag-specific CD4⁺ T cells were localized using Imaris built-in spot detection function and distance from T cell area centre was calculated and normalized for T cell are volumes. **f**, A T cell cluster was defined as a minimum of 3 T cells aggregating within closest distance of 15 μm measured from cell centroids (see Materials and Methods). Cell clusters of less than 3 cells were manually removed.

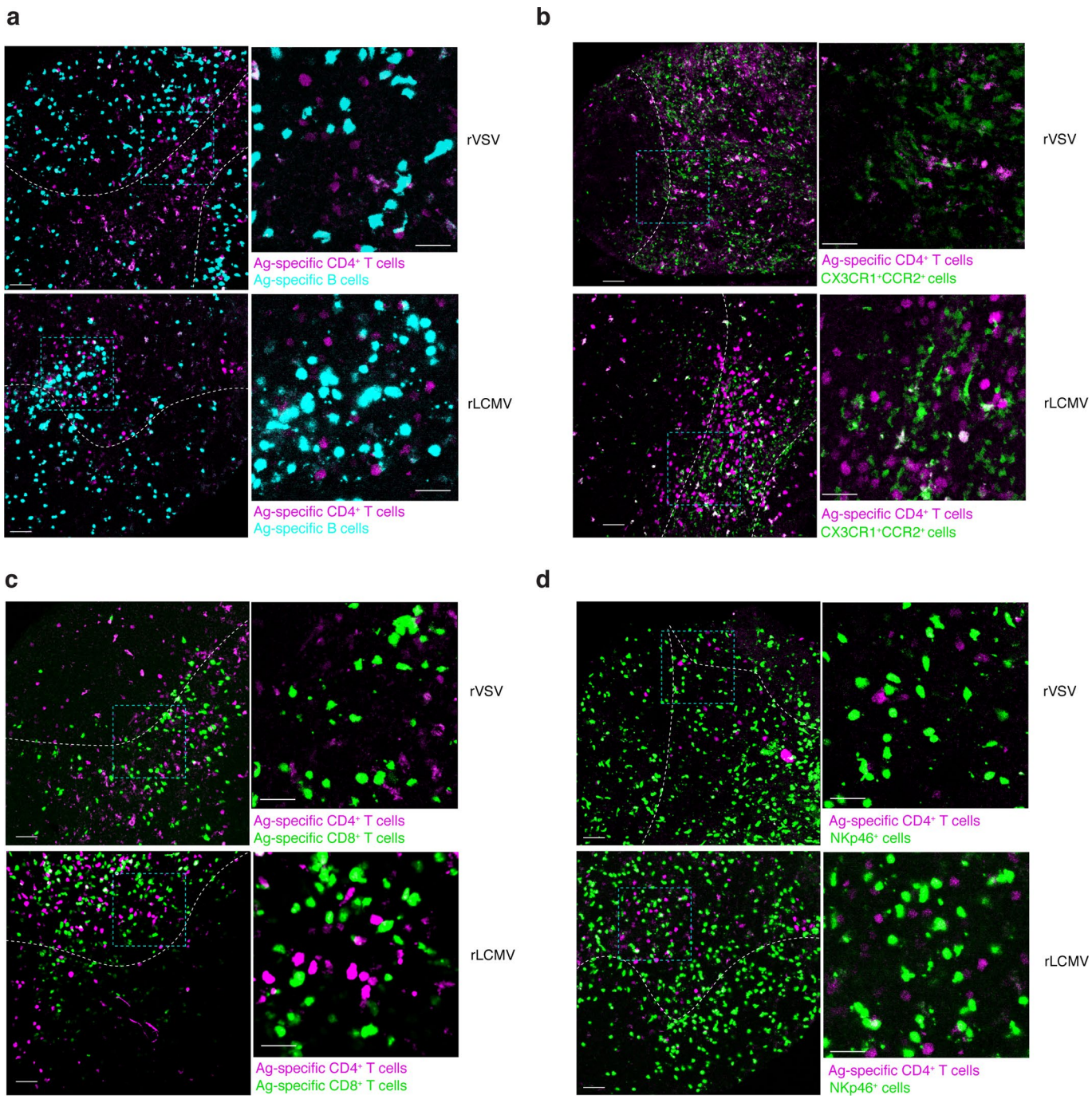

Extended Data Fig. 3 | Confocal analysis of the CD4+ T cell priming niche. Confocal imaging of murine dLNs collected 2 days after rVSV or rLCMV infection. Dashed lines represent the edges of B cell follicles and were depicted based on B220 staining. **a**, Ag-specific GFP+ CD4+ T cells (SMARTA, depicted in purple) and Ag-specific CFP+ B cells (KL25, depicted in cyan) were adoptively transferred into WT mice. **b**, Ag-specific CFP+ CD4+ T cells (SMARTA, depicted in purple) were adoptively transferred into CX3CR1-GFP x CCR2-RFP mice. A colocalization channel for GFP and RFP was used to depict inflammatory monocytes (cells positive for both CX3CR1 and CCR2, in green). **c**, Ag-specific CFP+ CD4+ T cells (SMARTA, depicted in purple) and Ag-specific GFP+ CD8+ T cells (P14, depicted in green) were adoptively transferred into WT mice. **d**, Ag-specific CFP+ CD4+ T cells (SMARTA, depicted in purple) were adoptively transferred into NKp46-ZsGreen mice. Scale bars represent 50 μm or 30 μm (zoom). The dotted square represents the zoomed area in the IFA where CD4+ T cell clusters are found. All images are representative of at least 2 independent experiments.

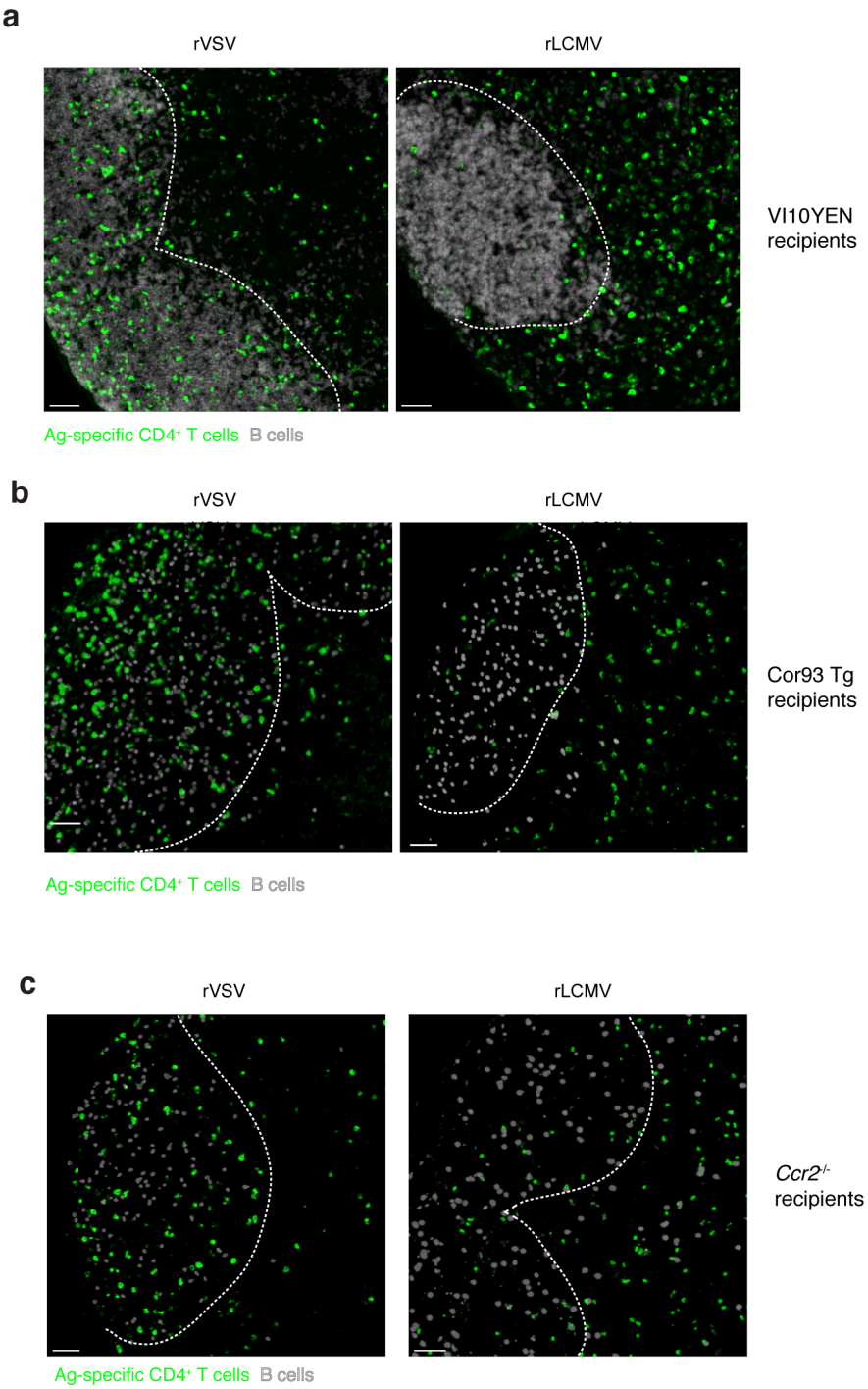

Extended Data Fig. 4 | Early antiviral CD4⁺ T cell localization is independent of Ag-specific B cells, Ag-specific CD8⁺ T cells and CCR2⁺ monocytes. Confocal imaging of dLNs of VI10YEN (**a**), Cor93 Tg TCR (**b**), and CCR2$^{-/-}$ (**c**) mice collected either 3 (**a**) or 5 (**b, c**) days after rVSV (*left*) or rLCMV (*right*) infection. Ag-specific CD4⁺ T cells are depicted in green. Dashed lines represent the edges of B cell follicles and were depicted based on polyclonal B cell positioning (**b, c**) or B220 staining (**a**) (both in grey). Scale bars represent 50 μm. Results are representative of at least 2 independent experiments.

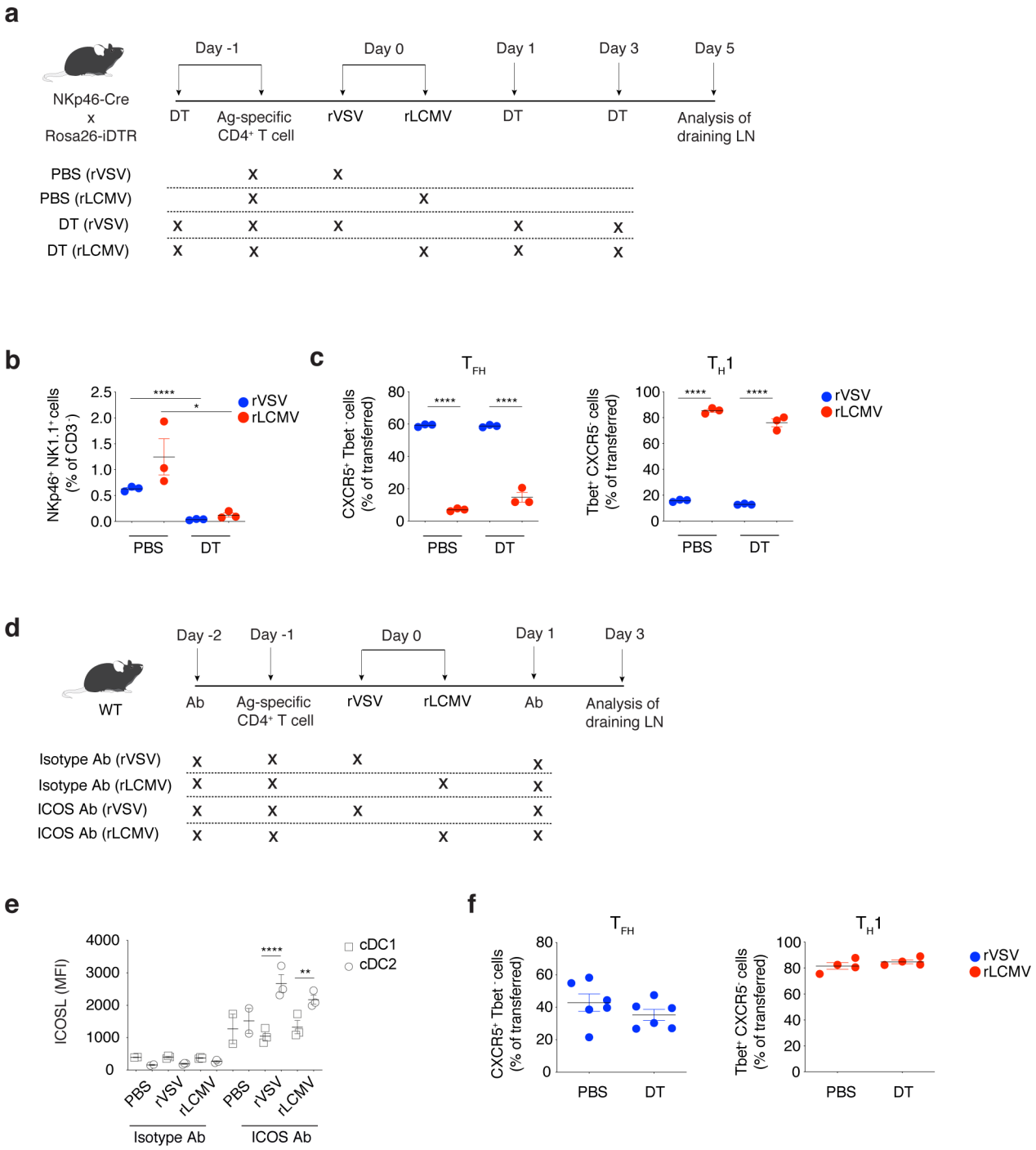

Extended Data Fig. 5 | Antiviral CD4⁺ T cell are primed by cDC2 cells and differentiate independently of NK cells. a, Schematic representation of the experimental procedure for the results described in panels **b** and **c**. 1×10^6 purified CD45.1⁺ Ag-specific (SMARTA) CD4⁺ T cells were injected into NKp46-DTR mice treated with PBS or DT as indicated. dLNs were collected 5 days after rVSV (blue) or rLCMV (red) infection. Percentages of NK cells (**b**), T_{FH} (**c**, *left*) and T_H1 (**c**, *right*) in dLNs were quantified by flow cytometry. Data are representative of 2 independent experiments. Mean+/- SEM is shown. $n=3$. A one-way Anova with Bonferroni's post-test was applied. * *p value* < *0.05;* **** *p value* < *0.0001* (**d**) Schematics of the experimental setup for the results described in panel **e**. 1×10^6 purified CD45.1⁺ Ag-specific (SMARTA) CD4⁺ T cells were transferred to WT mice treated with anti-ICOS blocking antibody or with isotype control, as indicated, prior to rVSV (blue) or rLCMV (red) infection. dLNs were collected 3 days after infection. **e**, ICOSL expression (mean fluorescent intensity) within CD11c⁺ MHC-II^{high} CD8⁺ (cDC1) and CD11c⁺ MHC-II^{high} CD11b⁺ (cDC2) cell subsets in dLNs of the mice described in **d**. Data are representative of 2 independent experiments. Mean+/- SEM is shown. PBS conditions $n=2$, all other conditions $n=3$. A one-way Anova with Bonferroni's post-test was applied. ** *p value* < *0.01;* **** *p value* < *0.0001*. **f**, 1×10^6 purified CD45.1⁺ Ag-specific (SMARTA) CD4⁺ T cells were transferred to WT and DT-treated XCR1-DTR mice prior to rVSV (blue, *left*) or rLCMV (red, *right*) infection. Quantification of T_{FH} (*left*) and T_H1 (*right*)—expressed as percentages of the total transferred cells—in dLNs 5 days after infection is shown. Mean ± SEM is shown. Data are representative of 2 independent experiments. $n=4$-6.

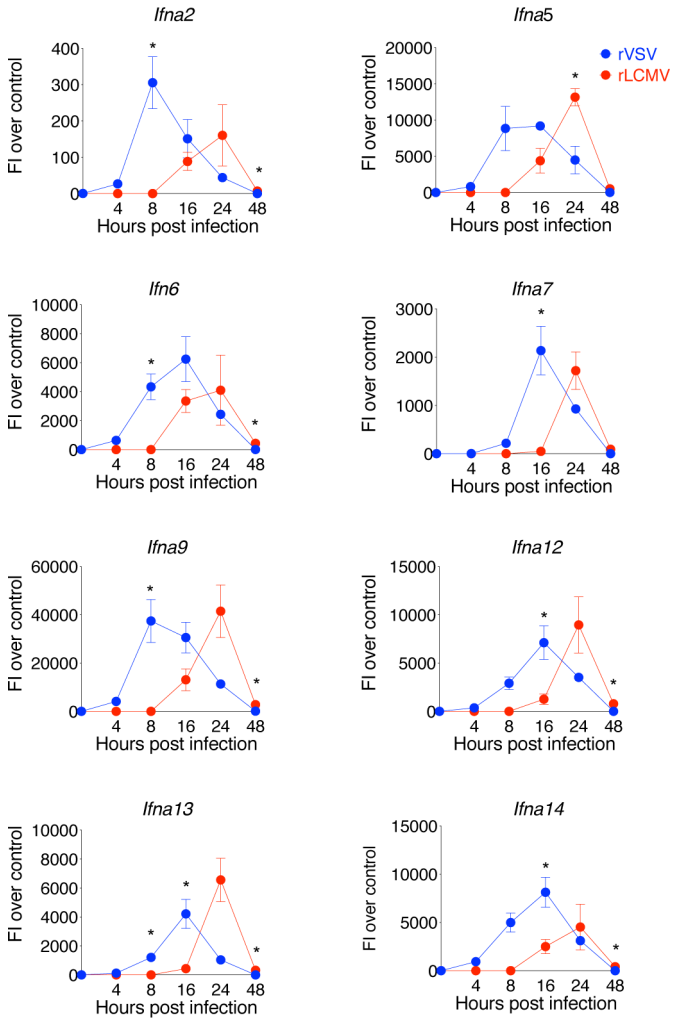

Extended Data Fig. 6 | Measurement of IFN-α isoforms upon rVSV and rLCMV infection. Analysis of *Ifna2, Ifna5, Ifna6, Ifna7, Ifna9, Ifna12, Ifna13, Ifna14* gene expression in dLN at 0, 4, 8, 16, 24 and 48 hours after rVSV (blue) or rLCMV (red) infection by qPCR. Data are pooled from 2 independent experiments. Mean± SEM is shown. 0 hours $n=3$; 4 hours $n=4$; 8 hours $n=3$ (rLCMV), 4 (rVSV); 16 hours $n=3$ (rLCMV), 4 (rVSV); 24 hours $n=2$ (rLCMV), 4 (rVSV); 48 hours $n=4$. A two-way Anova with LSD post-test was applied. * *p value* < *0.05*. The same sample was measured repeatedly for the 4 genes.

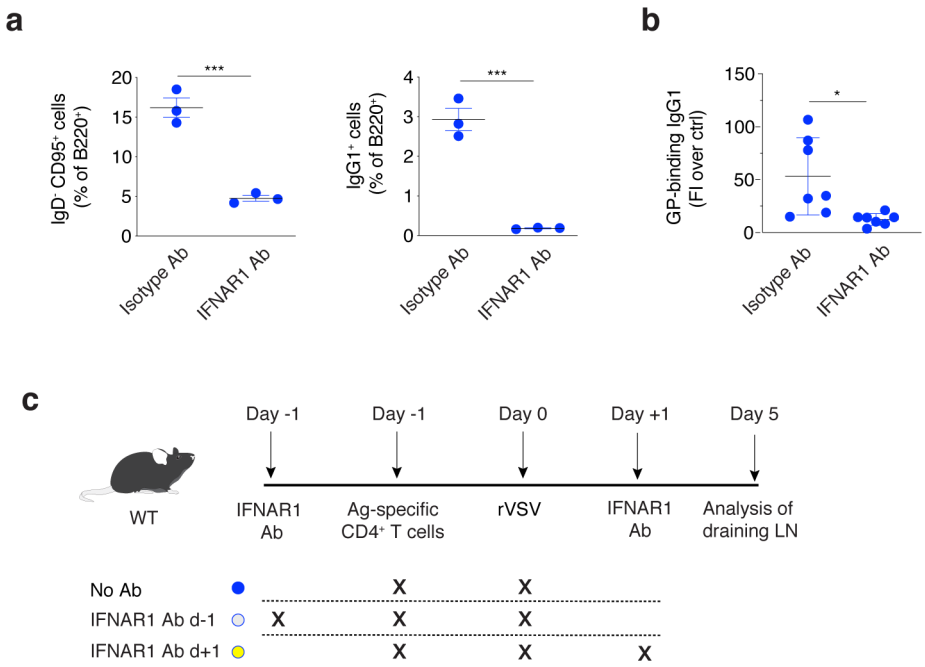

Extended Data Fig. 7 | Early type I IFN signalling promotes germinal centre B cells and antiviral antibody responses. a, Quantification of IgD$^-$ CD95$^+$ germinal centre (GC) B cells (left)—expressed as percentage of B220$^+$ cells—and of IgG1$^+$ cells (right)—expressed as percentage of B220$^+$ B cells—in the dLNs of mice treated with anti-IFNAR blocking antibody (or isotype control), and infected with rVSV 14 days earlier. Mean +/- SEM is shown. $n = 3$. An unpaired two-tailed t test was applied. *** p *value* < *0.001*. **b**, GP-binding IgG1 Abs (expressed as fold induction over uninfected controls) were measured in the sera of mice described in panel A, 14 days after rVSV infection. Data are pooled from 2 independent experiments. Mean ± SEM is shown. $n = 7$. An unpaired two-tailed t test was applied. * p *value* < *0.05*. **c**, Schematic representation of experimental procedure for the results described in Fig. 3d–f. 1×10^6 purified CD45.1$^+$ Ag-specific (SMARTA) CD4$^+$ T cells were transferred to CD45.2$^+$ WT recipients and treated anti-IFNAR1 blocking antibody either 1 day prior to (light blue) or 1 day after (yellow) rVSV infection.

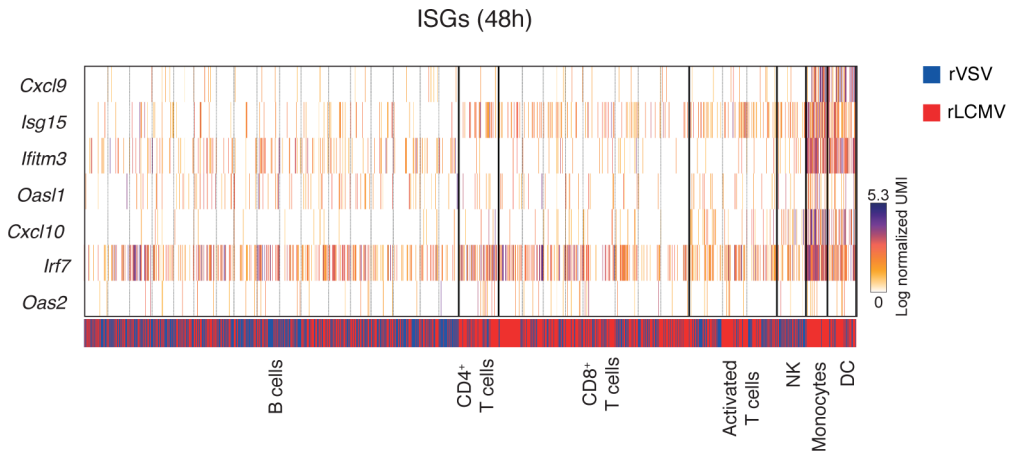

Extended Data Fig. 8 | Expression of interferon stimulated genes within the cellular components of the CD4⁺ T cell priming niche. Expression of the indicated interferon-stimulated genes (ISGs) within the cellular components of the photoactivated CD4⁺ T cell priming niches of the mice described in Fig. 2d–f. The colour bar on the bottom indicates each cell's origin (blue: photoactivated cells from rVSV; red: photoactivated cells from rLCMV).

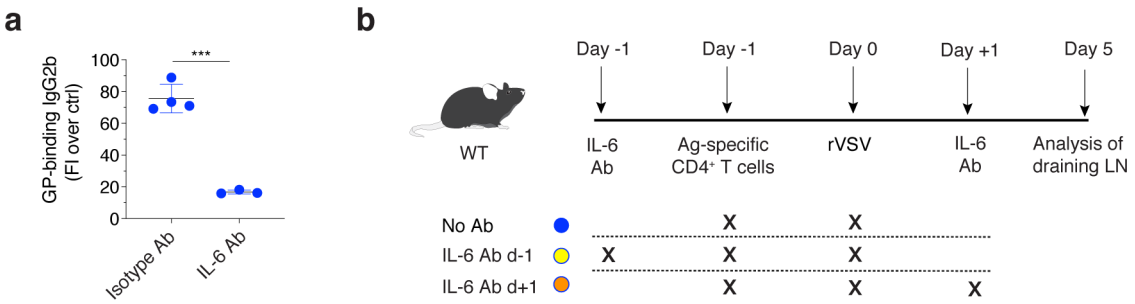

Extended Data Fig. 9 | Blocking IL-6 impairs antiviral antibody responses. a, WT mice were treated with anti-IL-6 blocking antibody (or isotype control) and sera were collected 14 days after rVSV infection. GP-binding IgG2b Abs were measured in the sera and expressed as fold induction over uninfected controls. Data are representative of 2 independent experiments. Mean ± SEM is shown. An unpaired two-tailed t test was applied. *** *p value* < *0.001*. **b**, Schematic representation of experimental procedure for the results described in Fig. 4e. 1×10^6 purified CD45.1$^+$ Ag-specific (SMARTA) CD4$^+$ T cells were transferred to CD45.2$^+$ WT recipients and treated with anti-IL-6 blocking antibody starting either 1 day prior to (yellow) or 1 day after rVSV infection (orange).

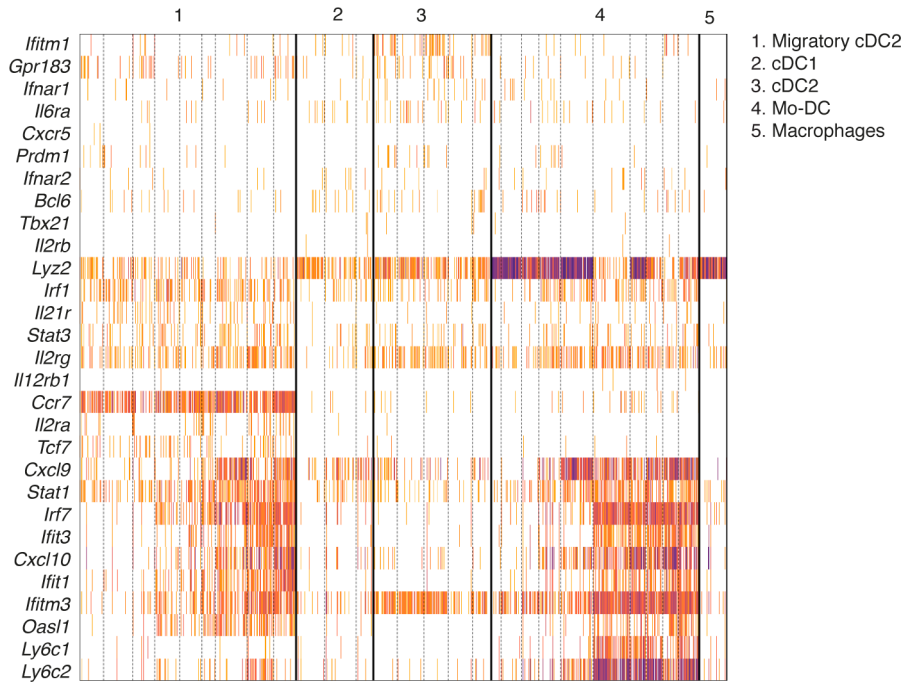

Extended Data Fig. 10 | Expression of interferon stimulated genes in dendritic cells. Expression of different ISGs across 2179 single QC positive CD11c^{+} MHC-II^{high} cells grouped in 5 clusters as described in the legend to Fig. 5a.

nature research

Corresponding author(s): Matteo Iannacone and Mirela Kuka

Last updated by author(s): Dec 23, 2019

Reporting Summary

Nature Research wishes to improve the reproducibility of the work that we publish. This form provides structure for consistency and transparency in reporting. For further information on Nature Research policies, see Authors & Referees and the Editorial Policy Checklist.

Statistics

For all statistical analyses, confirm that the following items are present in the figure legend, table legend, main text, or Methods section.

n/a	Confirmed	
☐	☒	The exact sample size (*n*) for each experimental group/condition, given as a discrete number and unit of measurement
☐	☒	A statement on whether measurements were taken from distinct samples or whether the same sample was measured repeatedly
☐	☒	The statistical test(s) used AND whether they are one- or two-sided *Only common tests should be described solely by name; describe more complex techniques in the Methods section.*
☒	☐	A description of all covariates tested
☐	☒	A description of any assumptions or corrections, such as tests of normality and adjustment for multiple comparisons
☒	☐	A full description of the statistical parameters including central tendency (e.g. means) or other basic estimates (e.g. regression coefficient) AND variation (e.g. standard deviation) or associated estimates of uncertainty (e.g. confidence intervals)
☐	☒	For null hypothesis testing, the test statistic (e.g. *F*, *t*, *r*) with confidence intervals, effect sizes, degrees of freedom and *P* value noted *Give P values as exact values whenever suitable.*
☒	☐	For Bayesian analysis, information on the choice of priors and Markov chain Monte Carlo settings
☒	☐	For hierarchical and complex designs, identification of the appropriate level for tests and full reporting of outcomes
☒	☐	Estimates of effect sizes (e.g. Cohen's *d*, Pearson's *r*), indicating how they were calculated

Our web collection on statistics for biologists contains articles on many of the points above.

Software and code

Policy information about availability of computer code

Data collection	BD FACSDiva Software v8.0.2 (BD Pharmingen) Leica Application Suite X (Leica Microsystems) ImSpector 6.4 (LaVision BioTec)
Data analysis	FlowJo 9.3 and FlowJo X (Treestar) Prism 5 (GraphPad Software) Imaris 9.0.2 (Bitplane) R package 5 MetaCell Python 3.5.0

For manuscripts utilizing custom algorithms or software that are central to the research but not yet described in published literature, software must be made available to editors/reviewers. We strongly encourage code deposition in a community repository (e.g. GitHub). See the Nature Research guidelines for submitting code & software for further information.

Data

Policy information about availability of data

All manuscripts must include a data availability statement. This statement should provide the following information, where applicable:

- Accession codes, unique identifiers, or web links for publicly available datasets
- A list of figures that have associated raw data
- A description of any restrictions on data availability

- All data is available in the main text or the supplementary materials.
- RNA-seq data that support the findings of this study have been deposited in the Gene Expression Omnibus (GEO) under accession code GSE130009.

Field-specific reporting

Please select the one below that is the best fit for your research. If you are not sure, read the appropriate sections before making your selection.

☒ Life sciences ☐ Behavioural & social sciences ☐ Ecological, evolutionary & environmental sciences

For a reference copy of the document with all sections, see nature.com/documents/nr-reporting-summary-flat.pdf

Life sciences study design

All studies must disclose on these points even when the disclosure is negative.

Sample size	Sample sizes were chosen based on prior research conducted in our laboratories to provide sufficient numbers of mice in each group to provide informative results and perform statistical testing
Data exclusions	In Niche-Seq experiments sequenced reads with multiple mapping positions were excluded, because their genomic origin could not be determined.
Replication	Biological replicates were used to ensure reproducibility of this study. All presented data are representative of at least 2 independent experiments with similar results. All result described in the study could be reproduced.
Randomization	Mice were matched for age and sex before randomization
Blinding	Blinding was not performed as not relevant in this study, because experiments with human samples and subjective measurement were not involved.

Reporting for specific materials, systems and methods

We require information from authors about some types of materials, experimental systems and methods used in many studies. Here, indicate whether each material, system or method listed is relevant to your study. If you are not sure if a list item applies to your research, read the appropriate section before selecting a response.

Materials & experimental systems

n/a	Involved in the study
☐	☒ Antibodies
☒	☐ Eukaryotic cell lines
☒	☐ Palaeontology
☐	☒ Animals and other organisms
☒	☐ Human research participants
☒	☐ Clinical data

Methods

n/a	Involved in the study
☒	☐ ChIP-seq
☐	☒ Flow cytometry
☒	☐ MRI-based neuroimaging

Antibodies

Antibodies used	- Antibodies used for flow cytometry or confocal microscopy were the following: anti-Bcl-6 (clone K112-91, Pharmingen #561524, 1:60), anti-T-bet (clone 4B10, Biolegend #644805, 1:60), anti-CXCR5 (clone 2G8, Pharmingen #560615, 1:100), anti-CD4 (clone RM4-5, eBioscience #48-0042, 1:100), anti-CD45.1 (clone A20, Biolegend #110716, 1:100), anti-CD45.2 (clone K104, Pharmingen #561874, 1:100), anti-CD44 (clone IM7, Biolegend #103032, 1:100), anti-IgD (clone 11-26C.2A, Biolegend #101224, 1:100), anti-NK1.1 (clone PK136, Biolegend #B207543, 1:100), anti-TCRb (clone H57-597, Biolegend #109229, 1:100), anti-CD8 (clone K53-6.7, Biolegend #100714, 1:100), anti-CD11c (clone N418, eBioscience #25-0114-82, 1:100), anti-CD11b (clone M1/70, Pharmingen #557960, 1:100), anti-I-Ab (MHC-II) (clone AF6-120.1, Biolegend #116416, 1:100), anti-IgG1 (clone MOPC-21, Biolegend #400119, 1:100), anti-CD95 (clone JO2, Pharmingen #557653, 1:100), anti-B220 (clone RA3-6B2, Biolegend #103229, 1:100), anti-CD69 (clone H1.2F3, Biolegend #104518, 1:100) and anti-CD25 (clone PC61, Biolegend #102008, 1:100). - Purified antibodies used in vivo were purchased from Bioxcell and included: InVivoMab anti-IFNAR (clone MAR-1 5A3, BioXcell #BE0241; 1 mg i.v.one day prior to or one day after infection), Mouse IgG1 isotype control (clone MOPC-21, BioXcell #BE0083), Anti-IL-6 (clone MP5-20F3, BioXcell #BE0046; 0.5 mg i.v. one day prior to or one day after infection and 0.25 mg every other day), Rat IgG1 isotype control (clone HRPN, BioXcell #BE0088), InVivoMab anti-ICOS (clone 7E.17G9, BioXcell #BE0059; 0.5mg i.v. two and one days prior to infection), Rat IgG2b isotype control (clone LTF-2, BioXcell #BE0092).
Validation	All antibodies were obtained from commercial vendors and we based specificity on descriptions and information provided in corresponding Data Sheets available and provided by the Manufacturers. Representative flow panels were shown in Fig. 1a, 1b, 3d, and Extended Data Fig. 1b.

Animals and other organisms

Policy information about studies involving animals; ARRIVE guidelines recommended for reporting animal research

Laboratory animals	C57BL/6, CD45.1 (inbred C57BL/6), β-actin-CFP (B6.129(ICR)-Tg(CAG- ECFP)CK6Nagy/J), β -actin-GFP [C57BL/6-Tg(CAG-EGFP)1Osb/J], Ccr2-/- (B6.129S4-Ccr2tm1Ifc/J), Rosa26-ZsGreen [B6.Cg-Gt(ROSA)26Sortm6(CAG-ZsGreen1)Hze/J] and PA-GFP mice were purchased from Charles River or from the Jackson Laboratory. LCMV-P14, SMARTA, Tg7, and Ifnar1-/- mice were obtained through the Swiss Immunological Mouse Repository (SwImMR, Zurich, Switzerland). Heavy chain knock-in and light chain BCR transgenic mice specific for VSV Indiana (VI10YEN) were obtained through the European Virus Archive. BCR transgenic mice specific for LCMV WE (KL25) bred against b-actin–DsRed were described. Cor93 TCR transgenic mice (lineage BC10.3, inbred CD45.1), in which > 98% of the splenic CD8+ T cells recognize a Kb-restricted epitope located between residues 93–100 in the HBV core protein (MGLKFRQL), have been previously described. XCR1-DTR-Venus, CD11c-cre and Ifnarfl/fl have been previously described. NKp46-Cre mice were obtained from Eric Vivier. Rosa26-iDTR mice were obtained from Marco Bacigaluppi. CX3CR1GFP/+ and CCR2RFP/+ mice were provided by I. Charo (University of California, San Francisco) by way of B. Engelhardt (University of Bern). Bone marrow chimeras were generated by irradiation of C57BL/6 mice with ~900 rad and reconstitution with the indicated bone marrow; mice were allowed to reconstitute for at least 8 weeks prior to use. Mice were housed under specific pathogen-free conditions and used at 8-10 weeks of age, unless otherwise indicated. In all experiments, mice were matched for age and sex before experimental manipulation.
Wild animals	No wild animals were used in the study
Field-collected samples	No field collected samples were included in the study
Ethics oversight	All experimental animal procedures were approved by the Institutional Animal Committee of the San Raffaele Scientific Institute.

Note that full information on the approval of the study protocol must also be provided in the manuscript.

Flow Cytometry

Plots

Confirm that:

☒ The axis labels state the marker and fluorochrome used (e.g. CD4-FITC).

☒ The axis scales are clearly visible. Include numbers along axes only for bottom left plot of group (a 'group' is an analysis of identical markers).

☒ All plots are contour plots with outliers or pseudocolor plots.

☒ A numerical value for number of cells or percentage (with statistics) is provided.

Methodology

Sample preparation	Sample preparation is described in the Materials & Methods section.
Instrument	BD FACS Canto or BD FACSARIA III
Software	BD FACS DIVA for acquisition and FlowJo (Treestar) for analyses
Cell population abundance	Cells were always at least 98% pure
Gating strategy	Gating strategies is indicated in the Figure legends and the Materials & Methods section.

☒ Tick this box to confirm that a figure exemplifying the gating strategy is provided in the Supplementary Information.